UNIVERSITÀ DEGLI STUDI DI PADOVA

Dipartimento di Fisica e Astronomia "Galileo Galilei"

Master Degree in Physics

Final Dissertation

Study of the $^{20}\mathrm{Ne}(p,\gamma)^{21}\mathrm{Na}$ reaction at astrophysical energies

Thesis supervisor

Dr. Antonio Caciolli

Candidate

Alessandro Compagnucci

Academic Year 2019/2020

ACKNOWLEDGEMENTS

We began as wanderers, and we are wanderers still.
We have lingered long enough on the shores of the cosmic ocean.
We are ready at last to set sail for the stars.

— *Carl Sagan,* Cosmos

Voglio ringraziare il mio relatore Antonio Caciolli per l'opportunità di lavorare con la collaborazione LUNA, i preziosi consigli e i calorosi incoraggiamenti. Grazie a Sandra Zavatarelli e Pietro Corvisiero della sezione di Genova per il supporto nello sviluppo delle simulazioni. Infine grazie ad Eliana Masha con cui ho condiviso il lavoro in questi mesi e Jakub Skowronski con cui ho passato la trasferta al Gran Sasso, la quarantena e con cui ho scambiato utili consigli.

CONTENTS

INTRODUCTION

The neon-sodium cycle is involved in the synthesis of Ne, Na, and Mg elements in stars and can take place in various astronomical sites such as hydrogen burning shells of red giant stars and asymptotic giant branch stars, in novae and in the core of massive stars. The $^{20}Ne(p,\gamma)^{21}Na$ is the first reaction of the cycle, and, having the slowest reaction rate, it controls the speed of the whole process. In particular, it was shown that a better assessment of this reaction might be crucial in explaining the anticorrelation between oxygen and sodium abundances exhibit by globular clusters. At astrophysical temperatures, the $^{20}Ne(p,\gamma)^{21}Na$ reaction rate is dominated by the high energy tail of a sub-threshold state at $E_R = -6.7$ keV, a direct capture component and a narrow resonance at $E_R = 366$ keV.

Measuring nuclear reactions at energies of astrophysical interest is often quite challenging because the cross sections are extremely low (less than 10^{-9} b). The Laboratory for Underground Nuclear Astrophysics (LUNA), situated at Laboratori Nazionali del Gran Sasso (LNGS), offers a unique opportunity to study this process thanks to the unprecedentedly low levels of background achieved in this location. Here proton capture on ^{20}Ne will be studied on a windowless gas target using two HPGe detectors. The detectors are shielded against environmental radioactivity by a copper and lead lining. The project focuses especially on the contribution from the $E_R = 366$ keV narrow resonance and the direct capture component below 400 keV.

This thesis illustrates the work made at the LUNA facility for the initial construction and characterization of the setup. Preliminary characterizations of both the environmental and beam induced background are presented. The beam calorimetry technique used to measure the proton beam current is exposed along with the methods used for its calibration.

The following analysis will then focus on Monte Carlo simulations made in order to optimize the geometry of the setup. A tuning of the positions of the detectors and the shielding is made using the available experimental data. The efficiency profile is then characterized for the two HPGe detectors. Finally, simulations of the resonant capture component of the reaction are provided. This allows us to determine the expected counting rate of the apparatus and probe the sensitivity to effects such as beam energy straggling inside the gas target.

1 ASTROPHYSICAL MOTIVATION

The energy is radiated by the stars mainly by means of the thermonuclear reactions happening inside the core [1]. A star originates when the interstellar gases, predominantly hydrogen and helium, condenses. Gravitational energy quickly makes the gas heat up and contract up until the thermal energy inside the core is high enough to ignite the burning of hydrogen by means of nuclear power. The energy released by these reactions is responsible for maintaining hydrostatic equilibrium up until the fuel in the core is exhausted and the burning of heavier and heavier elements starts.

In the next section, the formalism that describes this kind of reaction is exposed. By far the most important quantity to extract for astrophysics is the thermonuclear reaction rate that is given in input to the stellar evolution models and defines the sites and moments for a particular reaction to take place. Later on, we will expose the main scenarios where our process of interest, $^{20}\mathrm{Ne}(p,\gamma)^{21}\mathrm{Na}$, takes place as well as the current state of the art measurements for the reaction.

1.1 THERMONUCLEAR REACTION BASICS

Considering a nuclear reaction between two massive particles $0+1 \rightarrow 2+3$, we can define the reaction rate [2] as the number of reactions for unit volume and time

$$r_{01} \equiv \frac{\mathcal{N}_{\mathcal{R}}}{Vt} = N_0 N_1 \nu \sigma(\nu), \tag{1}$$

where $N_0 \equiv \mathcal{N}_t/V$ and $N_1 \equiv \mathcal{N}_b/V$ are the number densities of interacting particles, ν their relative velocity, and $\sigma(\nu)$ the cross section of the reaction. In the stellar plasma, at thermodynamic equilibrium, the relative velocity of the interacting nuclei is not constant and therefore we should talk about the probability distribution $P(\nu)d\nu$ for a particle of having velocity between ν and $\nu + d\nu$ with the proper normalization,

$$\int_0^\infty P(\nu)d\nu = 1. \tag{2}$$

This leads us to the generalization of the reaction rate for a distribution of relative velocities:

$$r_{01} = N_0 N_1 \int_0^\infty \nu P(\nu)\sigma(\nu)d\nu \equiv N_0 N_1 \langle \sigma\nu \rangle_{01}, \tag{3}$$

where $\langle\sigma v\rangle_{01}$ is the reaction rate per particle pair. The definition above can be further generalized to

$$r_{01} = \frac{N_0 N_1 \langle\sigma v\rangle_{01}}{1+\delta_{01}}, \tag{4}$$

where the Kronecker δ_{01} accounts for equal initial species in the reaction. In non-degenerate plasma at thermodynamic equilibrium the relative velocity of the two nuclei is given by the Maxwell-Boltzmann distribution

$$P(v)dv = \left(\frac{\mu}{2\pi k_B T}\right)^{3/2} e^{-\mu v^2/(2k_B T)} 4\pi v^2 dv \tag{5}$$

where $\mu = m_0 m_1/(m_0+m_1)$ is the reduced mass of the interacting particles, k_B the Boltzmann constant, and T the temperature of the star. Assuming $E = \mu v^2/2$ we may write Eq. 5 as

$$P(E)dE = \frac{2}{\sqrt{\pi}} \frac{1}{(k_B T)^{3/2}} \sqrt{E} e^{-E/k_b T} dE, \tag{6}$$

using this result the reaction rate per particle pair becomes:

$$\begin{aligned} \langle\sigma v\rangle &= \int_0^\infty \sqrt{\frac{2E}{\mu}} \sigma(E) P(E) dE \\ &= \left(\frac{8}{\pi\mu}\right)^{1/2} \frac{1}{(k_b T)^{3/2}} \int_0^\infty E\sigma(E) e^{-E/k_B T} dE. \end{aligned} \tag{7}$$

This equation fully characterizes the reaction rate at a given T, and therefore must be evaluated as a star evolve and its temperature changes.

Inside the stellar plasma, the energy of the nuclei is much lower than the Coulomb barrier between them and reactions usually happen through quantum tunneling. The cross section for this type of reaction drops exponentially at low energies and can be parameterized as

$$\sigma = \frac{1}{E} S(E) \exp\left(-\frac{2\pi}{\hbar}\sqrt{\frac{\mu}{2E}} Z_0 Z_1 e^2\right) = \frac{1}{E} S(E) e^{-2\pi\eta}, \tag{8}$$

Where Z_0 and Z_1 are the atomic charges of the target and the projectile, e the fundamental charge, η is the *Sommerfield parameter*, $e^{-2\pi\eta}$ (*Gamow factor*) accounts for the s-wave Coulomb barrier transmission probability and $S(E)$ is a smoothly varying function of the energy known as *S-factor*, which depends on nuclear effects.

Using the above definition the eq. 7 becomes

$$\langle\sigma v\rangle = \left(\frac{8}{\pi\mu}\right)^{1/2} \frac{1}{(k_b T)^{3/2}} \int_0^\infty S(E) e^{-2\pi\eta} e^{-E/k_B T} dE, \tag{9}$$

The terms $e^{-2\pi\eta}$ and $e^{-E/K_B T}$ defines a region known as *Gamow peak*, shown in Fig. 1, in this region the integrand of Eq. 9 has its maximal contribution to the reaction rate.

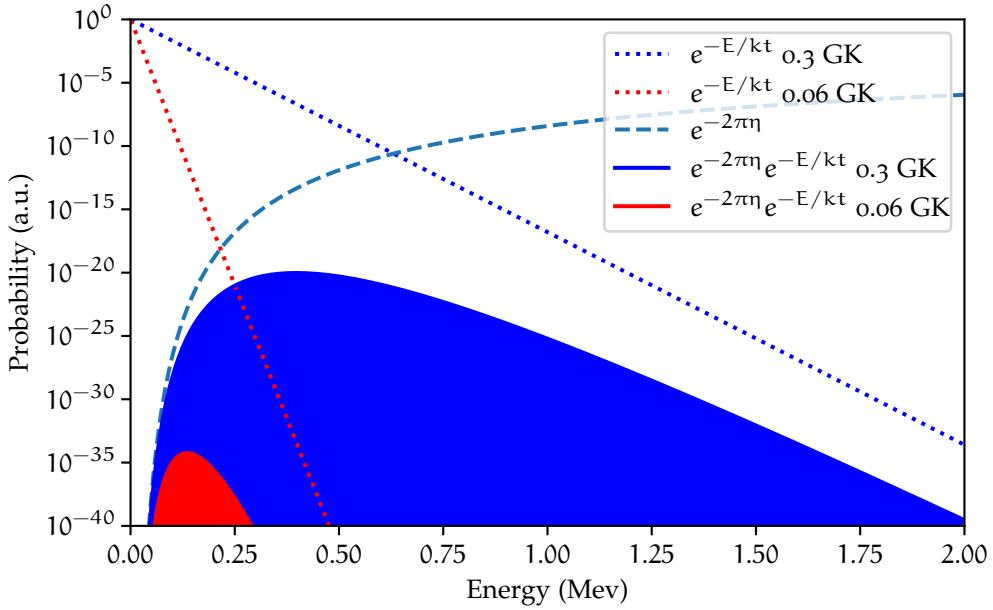

Figure 1: Gamow peak for the $^{20}Ne(p,\gamma)^{21}Na$ at two different temperatures. $T = 0.3$ GK refers to typical temperatures of interest for the nucleosynthesis in classical novae, $T = 0.06$GK is associated with hot hydrogen burning in massive stars.

1.1.1 Radiative capture reactions

Reactions induced by charged particles of the type $A(x,\gamma)B$, as our reaction of interest $^{20}Ne(p,\gamma)^{21}Na$, can proceed either through *direct capture* or *resonant capture* (Fig. 2). The direct process is characterized by the immediate transition to a bound state with the emission of a photon, in this case, the reaction cross section is proportional to a single matrix element,

$$\sigma_\gamma \propto |\langle B|\, H_\gamma\, |A+x\rangle|^2, \tag{10}$$

where H_γ is an electromagnetic operator describing the transition. The cross section of reactions going through direct capture can occur at all projectile energy and have typically a smooth energy dependence (i. e. Eq. 8).

Resonant radiative capture is a type of process that can happen when the sum of the projectile energy in the center of mass E_R and the Q-value of the reaction is equivalent to the energy E_x of an excited state the resulting compound nucleus,

$$E_x = E_R + Q. \tag{11}$$

When this happens the reaction cross section happens to be proportional to two factors, the contribution from the formation of the compound nucleus in the excited state and the one from the de-excitation into a final state of energy E_f,

$$\sigma_\gamma \propto |\langle E_f|\, H_\gamma\, |E_R\rangle|^2 |\langle E_R|\, H_x\, |A+x\rangle|^2, \tag{12}$$

the proportionality to this matrix elements are typically expressed using the partial width terms Γ_a and Γ_b, which accounts for the compound forma-

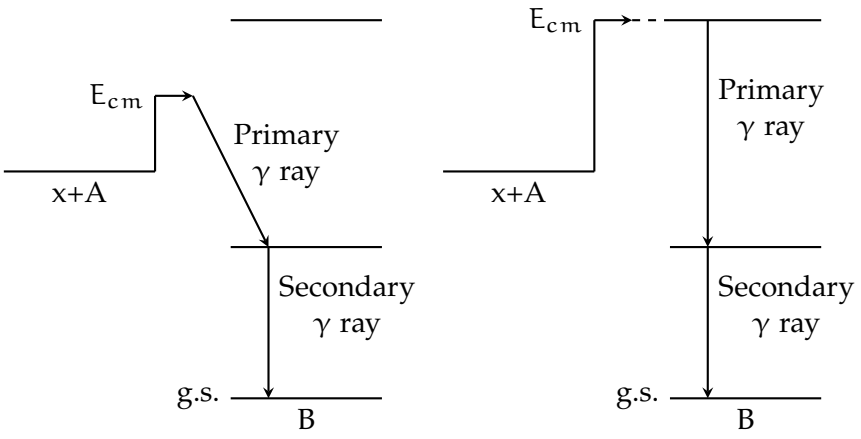

(a) Direct Capture **(b)** Resonant reaction

Figure 2: Energy level diagrams illustrating the Direct Capture (DC) and resonant reaction mechanisms.

tion and decay. When this type of process occurs the reaction cross section changes sharply. For this kind of reactions the cross section can be described by the Breit-Wigner formula:

$$\sigma(E)_{BW} = \pi\lambda^2 \frac{2J+1}{(2j_1+1)(2j_2+1)}(1+\delta_{01})\frac{\Gamma_a\Gamma_b}{(E-E_R)^2+(\Gamma/2)^2}, \tag{13}$$

where:

- $\lambda = 2\pi\hbar/\sqrt{2\mu E}$ is the de Broglie wavelength of the projectile in the center of mass system.
- j_1 and j_2 are the spins of the interacting particles and J is the spin of the excited state populated in the compound nucleus.
- $(1+\delta_{01})$ takes into account the possibility of target and the projectile being the same particle.
- $\Gamma = \Gamma_a + \Gamma_b + \ldots$ is the total width, accounting for all the open decay channels.
- E_R is the resonance energy in the center of mass frame.

If we are in the condition $\Gamma \ll E_R$ the resonance is defined as *narrow*. In this situation we can approximate Eq. 7 considering that the factor Ee^{-E/k_BT} changes very little inside the resonance region, therefore can be taken outside the integral with $E = E_R$:

$$\langle\sigma v\rangle = \left(\frac{8}{\pi\mu}\right)^{1/2} \frac{1}{(k_bT)^{3/2}} E_R e^{-E_R/k_BT} \int_0^\infty \sigma(E)_{BW} dE. \tag{14}$$

The integration of the Breit-Wigner, assuming a negligible dependence in energy of the partial widths, yields

$$\int_0^\infty \sigma(E)_{BW} dE = 2\pi^2\lambda^2\omega\gamma, \tag{15}$$

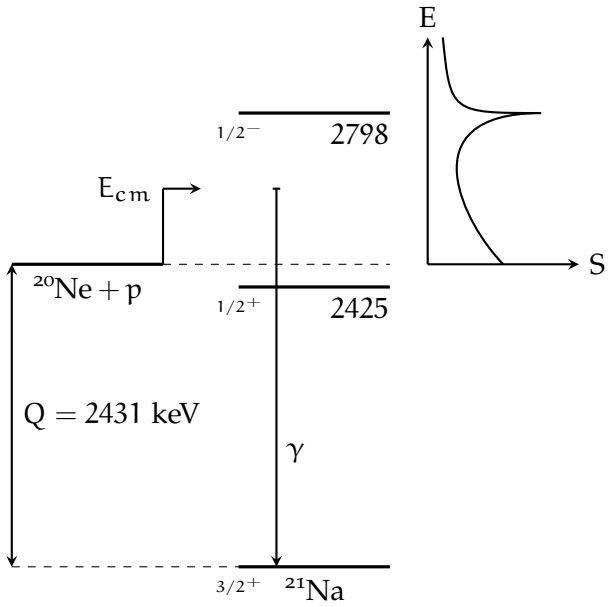

Figure 3: Level scheme of ^{21}Na with the entrance channel of $^{20}\mathrm{Ne}+\mathrm{p}$. The behavior of the S-factor is also shown, in particular the contributions from the level at $E_X = 2425$ keV (*subthreshold resonance*) and $E_{res} = 2798$ keV (*narrow resonance*). Only the example transition to the ground state is shown here.

where

$$\omega\gamma = \frac{2J+1}{(2j_1+1)(2j_2+1)}(1+\delta_{01})\frac{\Gamma_a\Gamma_b}{\Gamma} \tag{16}$$

is the *resonance strength* and expresses the integrated resonance. As said the former calculations are valid in the context of a narrow resonance, this is not always the case.

If the resonance is relatively broad ($\Gamma/E_R \geqslant 0.1$) we need to take into account the energy dependence of the widths and Eq. 14 has to be modified making the substitution:

$$\sigma_{BW}(E) = \sigma(E_R)\frac{E_R}{E}\frac{\Gamma_a(E)}{\Gamma_a(E_R)}\frac{\Gamma_b(E)}{\Gamma_b(E_R)}\frac{(\frac{1}{2}\Gamma(E_R))^2}{(E-E_R)^2+(\frac{1}{2}\Gamma(E))^2}, \tag{17}$$

where $\sigma(E_R)$ is the cross section evaluated at the resonance energy.

If we consider now states where $E_R = E_X - Q$ is negative the phenomenon of *subthreshold resonance* (Fig. 3) might also take place, this is directly related to the fact that any state has a finite lifetime and thus a finite width $\Gamma \approx \hbar/\tau$. This mechanism of interaction affects the low energy tail of the S-factor and, consequently, the thermonuclear reaction rate at relatively low temperatures. We will see that this is the case for the $^{20}\mathrm{Ne}(p,\gamma)$, as ^{21}Na has an excited state just below the Q-value of the reaction ($E_R = -6.4$ keV), with a corresponding γ width of $\Gamma_\gamma = 0.17 \pm 0.05$ eV [3].

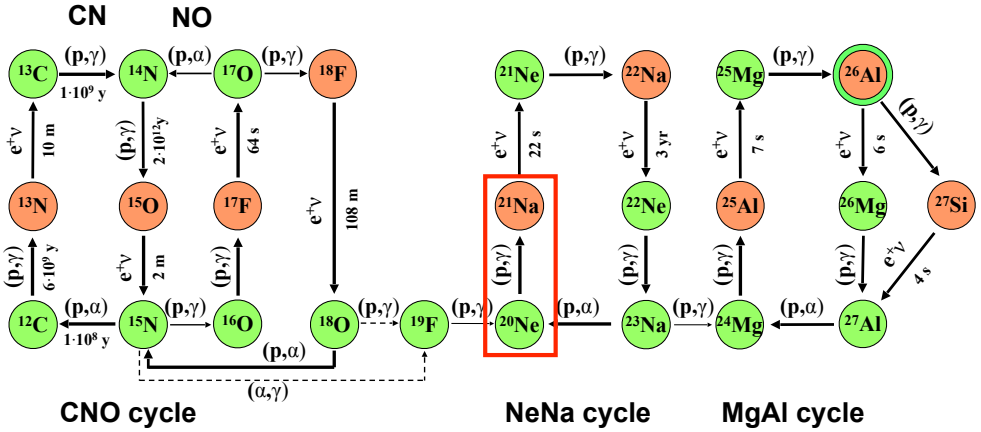

Figure 4: Hydrogen burning cycles beyond the pp-chain. The $^{20}Ne(p,\gamma)^{21}Na$ reaction, part of the NeNa cycle, is highlighted in red. Original image taken from [4].

1.2 NUCLEOSYNTHESIS IN THE STARS

Hydrogen burning in the stars happens mainly via the proton-proton chain and the CNO cycle. The pp-chain mechanism is dominant at lower temperatures whereas in stars more massive than 1.2 $M_\odot$ the CNO cycle dominates as a source of energy.

The CNO cycle (pictured in Fig. 4 along with the other reaction involved in hydrogen burning) requires the presence of some isotopes of carbon, oxygen and nitrogen that acts as a catalyst meaning that the heavier elements are not consumed, while one helium is produced in this process through a series of proton capture reactions and β-decays involving 4 hydrogens. Depending on the temperature regime different branches of the CNO cycle are activated [5], for example at low temperature (T ~ 40 MK) only the CN cycle is active whereas at higher temperatures the NO cycle is active as well.

In massive stars and higher temperature environments the so-called hot CNO cycle can proceed through many pathways and other reactions can take place, including the NeNa and MgAl cycles.

1.2.1 AGB stars and Globular Cluster features

The *Asymptotic Giant Branch* (AGB) phase of stellar evolution begins following the helium burning of low to intermediate mass stars, AGB stars consist of a degenerate carbon-oxygen core, an He intershell, an H shell, and an expanded convective envelope (see Fig. 5).

During this phase, CNO cycling in the H shell provides the energy, while recurrently being interrupted by the activation of the helium burning at the bottom of the inner shell (*thermal pulses*). When this happens convection is established in the region in between the two shells and the hydrogen burning stops. During thermal pulses the convective envelope can penetrate inside the hydrogen, bringing the synthesized materials to the surface in a phenomenon know as *Third Dredge Up* (TDU). For this reason, AGB stars are

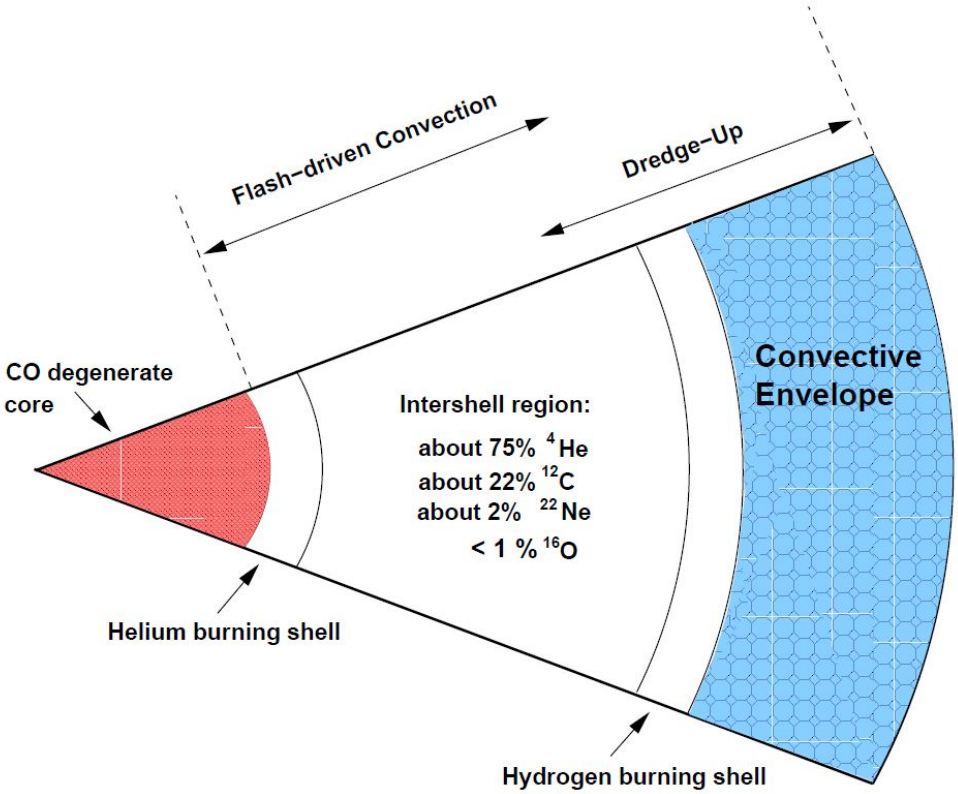

Figure 5: The structure of AGB stars. Taken from [6].

widely regarded as responsible for the pollution of the interstellar medium with p-capture nucleosynthesis material [7].

In the more massive AGB stars ($M > 4\ M_{\odot}$), depending on the metallicity, the base of the hydrogen burning region can become hot enough ($T > 60$ MK) to activate efficient CNO cycling or, for the most massive AGB stars the aforementioned NeNa and MgAl cycles (*Hot Bottom Burning*, HBB) [8]. The reactions involved in this cycles (see Fig. 4) have become increasingly important as they are believed to be the main actors involved in explaining the observed anticorrelation between O-Na and Al-Mg observed by stars of Galactic globular clusters (review in [9]).

Globular Clusters (GC) are tightly packed, gravitationally bound, collection of stars in spherical distributions. The canonical approach to these objects is to describe them as formed at the same time in chemically homogeneous conditions and in the same region of space.

On contrast, it was later discovered that the abundances for the lighter elements within GC stars change a lot, later on high-resolution spectroscopy revealed the O-Na and Mg-Al anticorrelations present in GC stars on the Red Giant Branch (Fig. 6) [11]. These evidences lead to the conclusion that the abundance variations could not be attributed to processes internal to the stars since the energies in play are too low and the convective envelopes too thin. The main idea is that this stars formed from hot H-burning enriched material from within the GC (*self enrichment*), several candidates might play a role in this process but currently AGB stars undergoing hot bottom burning are one of the main candidates.

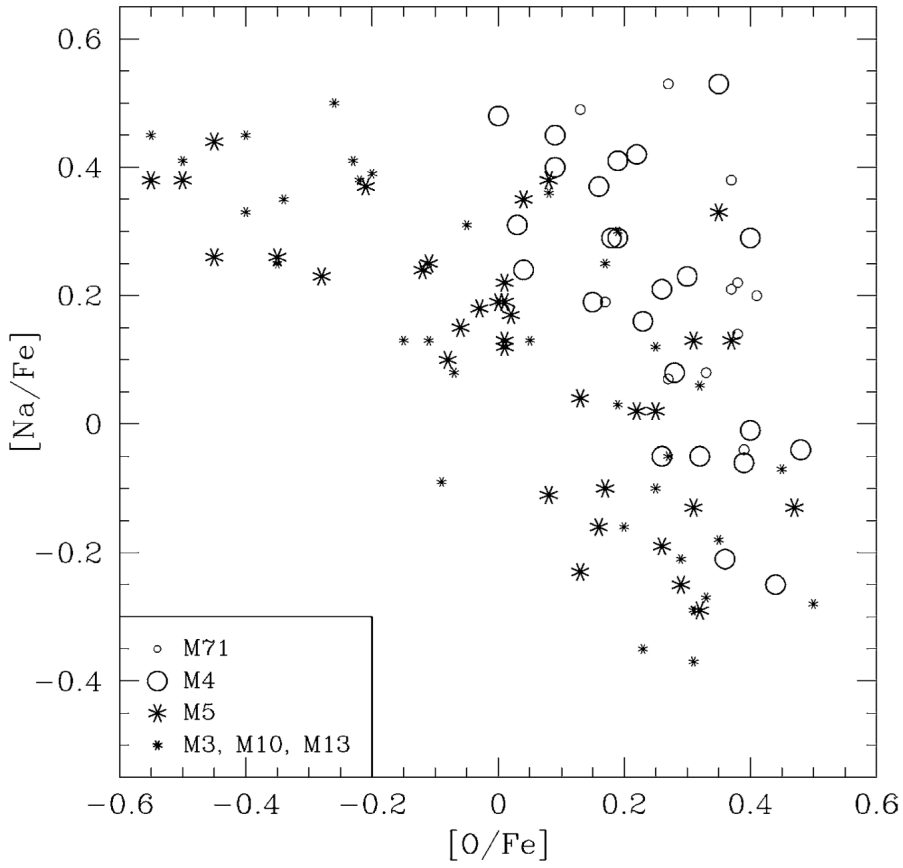

Figure 6: Anticorrelation between sodium and oxygen relative abundances for cluster of intermediate metallicity. Taken from [10].

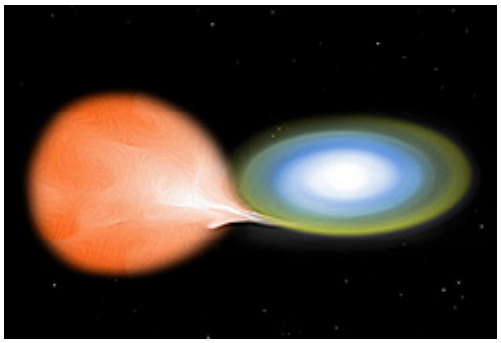

Figure 7: Artist's rendition of a white dwarf accreting hydrogen from their companion star.

In order to better address this problem, it is then necessary to have a better understanding of the reaction rates involved in this type of processes.

1.2.2 Classical novae

At the end of the life of low and intermediate mass stars ($M < 14\ M_\odot$) they experience several thermal instabilities following their AGB or super-AGB phase. At the end of this process they lose their envelopes and what remains, typically their degenerate CO core or ONe for more massive ones, is usually referred to as a *White Dwarf* (WD).

When a WD is gravitationally bounded in a close binary system with an H-rich main sequence star, they may start to accrete material on their surface (Fig. 7). At one point, when enough material is accumulated, thermonuclear reaction ignites leading eventually to a Novae explosion [12].

Depending on the initial WD mass and the accretion rate either a *type Ia supernovae explosion* or a *classical novae* may take place. Type Ia supernovae explosion happens if the mass of the white dwarf reaches the Chandrasekhar limit ($1.4\ M_\odot$), in this case the whole white dwarf is destroyed. In contrast in classical novae only the outer white dwarfs envelope is ignited and expelled, and this phenomenon may eventually start over again.

During this explosive events temperature at the bottom of the H-rich envelope may reach temperatures as high as 400 MK igniting the hot CNO cycle and the nucleosynthesis via proton capture involving heavier elements [13] and therefore enriching the expelled material with the product of the reaction involved.

1.3 THE NEON–SODIUM CYCLE

The Neon-Sodium cycle contributes to the hydrogen burning, allowing the conversion of 4 protons into helium inside the stars. This is accomplished by means of a series of proton captures and beta decays, the sequence of reaction involved is:

$$^{20}\mathrm{Ne}(p,\gamma)^{21}\mathrm{Na}(\beta^+,\nu)^{21}\mathrm{Ne}(p,\gamma)^{22}\mathrm{Na}(\beta^+,\nu)^{22}\mathrm{Ne}(p,\gamma)^{23}\mathrm{Na}(p,\alpha)^{20}\mathrm{Ne}. \quad (18)$$

These processes are not very strong sources of energy for the stars, however, are crucial in the synthesis of elements between ^{20}Ne and ^{24}Mg, in particular the $^{22}Ne(p,\gamma)^{23}Na$ reaction is responsible for and increase of elemental Na by a factor 10 [14].

This cycle might take place inside the hydrogen burning shell of red giant stars, Asymptotic Giant Branch (AGB) stars, novae, and in the core of massive stars. Evidence of this has been found in various astrophysical sites [15, 16].

Moreover, as briefly mentioned in 1.2.1, one recent problem in astrophysics is explaining the Oxygen-Sodium (O-Na) anticorrelation observed in Globular Clusters (GC). The current AGB stellar models seem unable to explain this feature exhibit by observations, at least using the available nuclear data [17]. In fact, after a better assessment of the contribution from the $^{22}Ne(p,\gamma)^{23}Na$ [18], it was recently shown that clearer estimations of $^{20}Ne(p,\gamma)^{21}Na$ and $^{23}Na(p,\alpha)^{20}Ne$, i. e. and the entrance and exit channel of the Ne-Na cycle, which are now the least understood, could lead to further improvements in the understanding of the ^{23}Na abundance problem in GC [19].

The $^{20}Ne(p,\gamma)^{21}Na$ is predicted to be the reaction with the slowest rate of Ne-Na cycle [20], and therefore the one that controls the speed at which the cycle proceeds.

1.4 $^{20}Ne(p,\gamma)^{21}Na$ REACTION

Proton capture on ^{20}Ne nuclei may occur in the aforementioned stellar environment if the temperature exceeds $T = 0.05$ GK [14]. A level scheme of the reaction (Q-Value = 2431.68 keV) is shown in Fig. 8a.

At temperature below 0.1 GK the reaction rate of the $^{20}Ne(p,\gamma)^{21}Na$ is dominated by the tail of a subthreshold resonance (Fig. 8b), the behavior of the S-factor at low energies can be well extrapolated knowing the (formal) reduced proton width for the 2425 keV level from (d,n) transfer reactions (see i. e. [2] pp.122).

At higher temperatures $T = 0.1 - 1$ GK the main contribution is from the direct capture process with various branchings. There is also a narrow resonance ($E_R = 366$ keV), corresponding to the excited state at $E_X = 2797.5$ keV of the ^{21}Na, in the energy region covered by the LUNA-400 accelerator. Until very recently the strength of this low energy resonance was only measured by Rolfs *et al.* in 1975 [22]. A new result from the TUNL group appeared in recent times, it is reported in the PhD thesis by Cooper [23], who gave a different result for this value.

Assessing the contribution of this resonance to the reaction rate will be one of the main goals of the experiment.

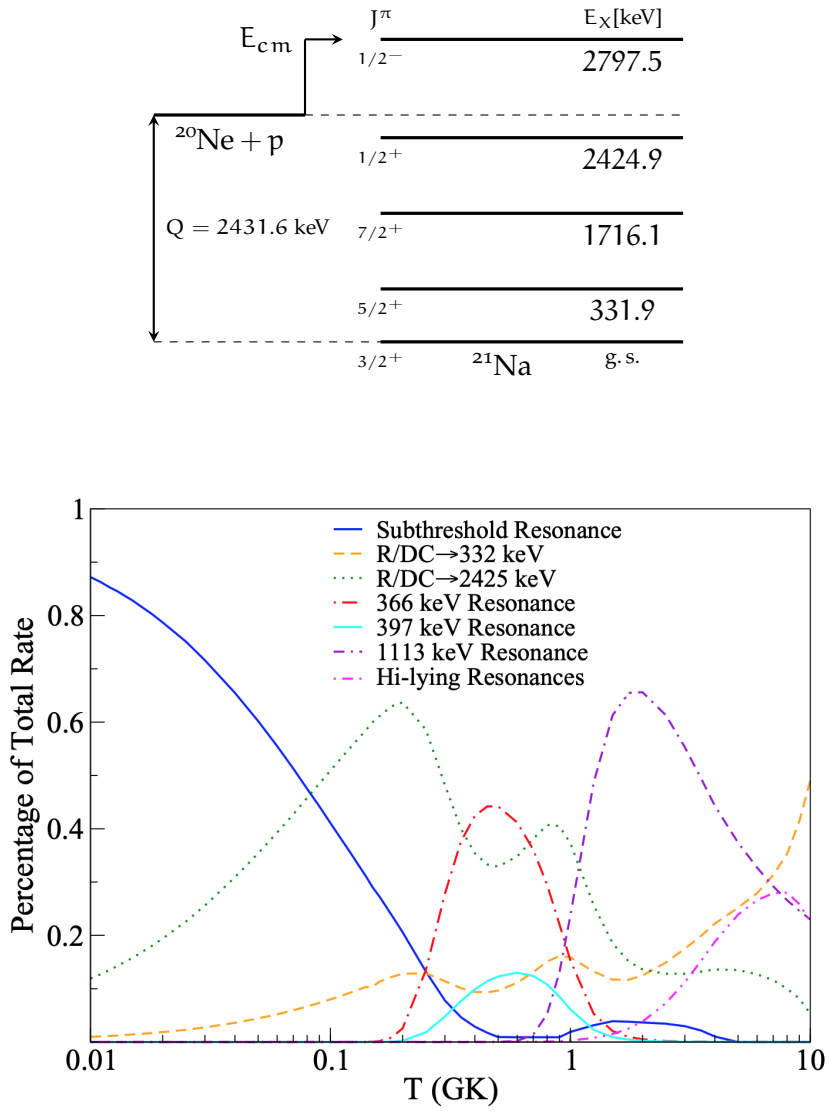

Figure 8: At the top a level scheme of the $^{20}Ne(p,\gamma)^{21}Na$, at the bottom the percentage contribution to the reaction rate from different processes at different temperature (Taken from [21]) .

1.4.1 $^{20}Ne(p,\gamma)^{21}Na$: state of the art

The $^{20}Ne(p,\gamma)^{21}Na$ reaction has already been studied experimentally by different groups [21–25] with both direct and indirect approaches.

Rolfs *et al.* (1975)

Rolfs *et al.* used a setup consisting of an extended windowless gas target with natural neon gas and two Ge(Li) detectors placed at 0° and 90° and shielded with lead. They reported cross section down to proton energy of 320 keV, measuring the contribution of transition to the ground state and to the 2424.9 keV and 331.9 keV excited states of ^{21}Na. They studied both the non resonant cross section and the $E_R = 366$ keV resonance reporting a strength $\omega\gamma = (0.11 \pm 0.02)$ meV [22].

Mukhamedzhanov *et al.* (2006)

In 2006 an indirect measurement was conducted by Mukhamedzhanov *et al.* using the $^{20}Ne(^3He, d)^{21}Na$ transfer reaction [24]. This experiment led to the extrapolation of the asymptotic normalization coefficient that was used to determine the proton partial width for the subthreshold resonance state and the DC contribution to the S-factor. Both these results was found to agree fairly well with the one given by Rolfs *et al.* .

Lyons *et al.* (2018)

Lyons *et al.* studied the reaction at the KN accelerator of the Notre Dame University. They used a neon implanted target on tantalum backing and studied the reaction over a wide range of energies ($E_p = 0.5 - 2$ MeV), interpreting the results in the R-matrix formalism. The resulting S-factor from this work is shown Fig.9, with the contribution from the direct capture to the ground state, the 332 keV state, and the 2425 keV subthreshold resonance. Their results were pretty much in agreement with the ones by Rolfs *et al.*, but they found an overall $\sim$ 20% reduction in the total reaction rate [21].

More recent measurements

Recently the reaction was also studied at TUNL and described in Cooper's PhD thesis [23]. Even these experiments were carried out using implanted targets on tantalum backings, the $E_R = 366$ keV was measured again and a different value of $\omega\gamma = (0.0722 \pm 0.0068)$ meV for the resonance strength was given. Cooper determined also different branching ratios for transitions to the excited states of ^{21}Na, in particular, the transition $R \rightarrow 332$ keV (measured by Rolfs to have a branching ratio of 11±4%) was not seen (see Tab. 1). This led to an update of the reaction rates. The origin of the discrepancy with the result given by Rolfs *et al.* was also further addressed in [23].

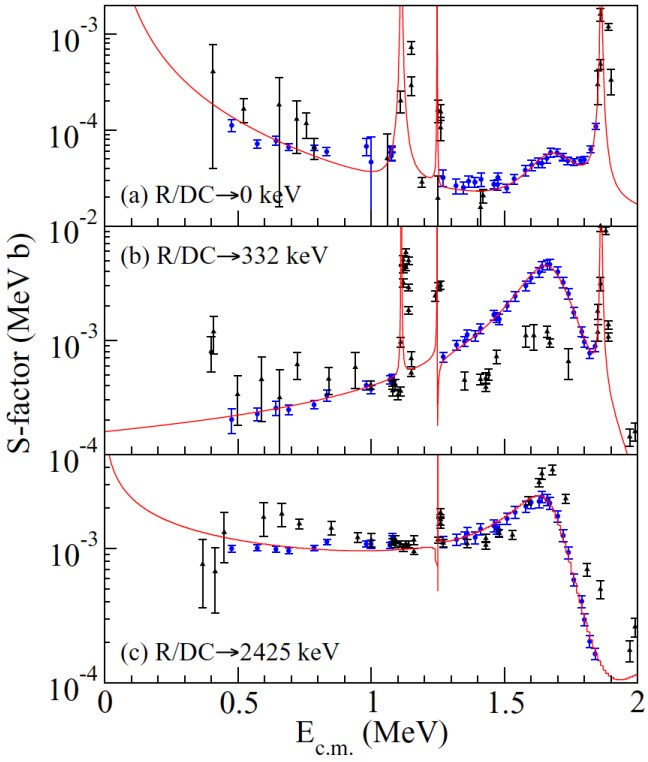

Figure 9: The astrophysical S-factor for the three transitions of interest as measured by Lyons *et al.* (in blue), with the results from [22] in black, and the R-matrix fit in red. Taken from [21]

	Cooper	Rolfs *et al.*
B.r. res $\rightarrow$ 2425	$61.5 \pm 7.3\%$	$56 \pm 4\%$
B.r. res $\rightarrow$ 332	1.6 ± 1.1 %	11 ± 4 %
B.r. res $\rightarrow$ gs	35.9 ± 5.3 %	33 ± 4 %
$\omega\gamma$	0.0722 ± 0.0068 meV	0.11 ± 0.02 meV

Table 1: Comparison between branching ratios and resonance strengths for the 366 keV resonance given by Rols *et al.* and Cooper

The last set of measurements found in later literature are very recent results reported in a PhD thesis by Karpesky [25] who studied the $^{20}Ne(p,\gamma)^{21}Na$ using the DRAGON facility at TRIUMF. The reaction was studied on inverse kinematic using a ^{20}Ne beam delivered to a windowless gas target and γ-rays were measured with a BGO scintillators array.

Karpesky measured a total of four reaction energies ranging from center-of-mass energies of 265.5 keV (within the astrophysical range of interest for ONe novae) to 519.6 keV, reporting the S-factor for the different transition of interest.

The discrepancies present in the literature, in particular the new $\omega\gamma$ and branchings reported by Cooper in his thesis, leads to the necessity of new measurements. In this case, the LUNA-400 accelerator is perfectly suited for the task of studying this reaction in the energy range of interest.

2 THE LUNA EXPERIMENT

Attempting direct measurements of radiative capture reactions at low energies can be extremely difficult. The first problem, as we have seen, is that the cross section drops exponentially below the Coulomb barrier, therefore measuring such a weak signal often requires a high intensity beam.

Another problem to take into account is the background, at the γ-ray energies of interest the main contributions are from the environmental radioactivity (mainly below 2.6 MeV) and cosmic radiation (dominant above 2.6 MeV). Environmental radioactivity is due to radioisotopes like the decay chain of uranium and thorium and the ^{40}K and can typically be attenuated shielding the setup, whereas cosmic radiation, typically in the form of muons, can deposit energy in the detector volume or interact with the surrounding materials producing radio-isotopes or neutrons, one way to overcome this problem is to go underground, where the muon flux is drastically reduced.

In this chapter the main components of the LUNA experiment are exposed, the experimental setup that will be used in the measurement of the ^{20}Ne$(p,\gamma)^{21}$Na is described and some initial considerations about its characterization are made based on the experimental data taken in February 2020 before the sanitary crisis and former measurements made with the same setup, including an evaluation of the environmental and beam-induced background, the final background reduction expected and a preliminary calibration of the calorimetric system used to measure the beam intensity. This initial characterization of the setup will be important for the development of the simulations, discussed in the last section of the thesis.

2.1 THE UNDERGROUND LUNA FACILITY

The Laboratory for Underground Nuclear Astrophysics (LUNA) is located in the Gran Sasso National Laboratories [26].

The main advantage of this peculiar location for the LUNA experiment is the substantial suppression of the background induced by *cosmic rays*. These high-energy charged particles, mainly protons (~90%) and α particles (~10%), coming from space interacts with nuclei in the upper atmosphere. When this happens they create a shower of particles (Fig. 10). Muons, created by the decay of charged pions, are the most penetrating component of the cosmic rays induced background, they lose energy inside the particles and γ-rays detectors and generate spallation neutron and radioactive nuclei in the surrounding materials.

Deep underground the setup is shielded by 1400 m of dolomite rock (3800 m of equivalent water), this allows the complete shielding of the hadronic component of cosmic rays as well as the suppression of the muonic component by about 6 orders of magnitude and 3 for neutrons compared to

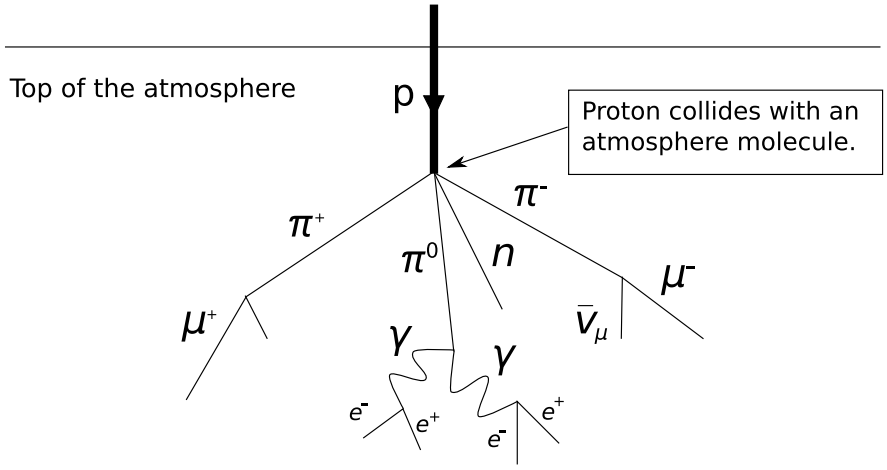

Figure 10: The interaction of cosmic rays in the upper atmosphere produce a shower of particle.

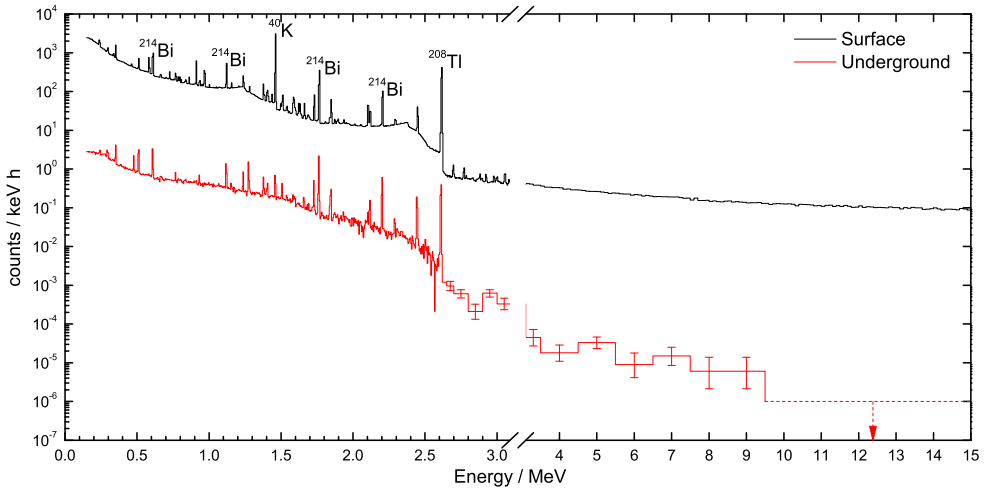

Figure 11: Comparison between γ-ray spectra taken with an HPGe detector at a surface laboratory and underground at LNGS, including proper shielding as discussed in section 2.1. Taken from [27].

earth surface [27]. For these reasons, the underground facility serves as an exceptional location to measure the tiny cross sections of interest (from pico to femto barn).

Figure 11 serves as a comparison between the γ-ray spectra obtained by High-Purity Germanium (HPGe) detector placed both underground and at the surface. The high energy component of the spectra is completely negligible in this condition, whereas the component of the spectra below 2.6 MeV is mainly due to environmental radioactivity. This part of the spectrum is occupied by the effects of long-lived radioisotopes, in particular the decay chains of ^{238}U and ^{232}Th and the ^{40}K.

The effect of radioactive nuclides can be mitigated using passive shielding, usually made of high Z materials like lead or copper. In this case, particular attention is made in selecting low-background lead brick and refined electrolytic copper to cope bremsstrahlung generated by β emitters, like the

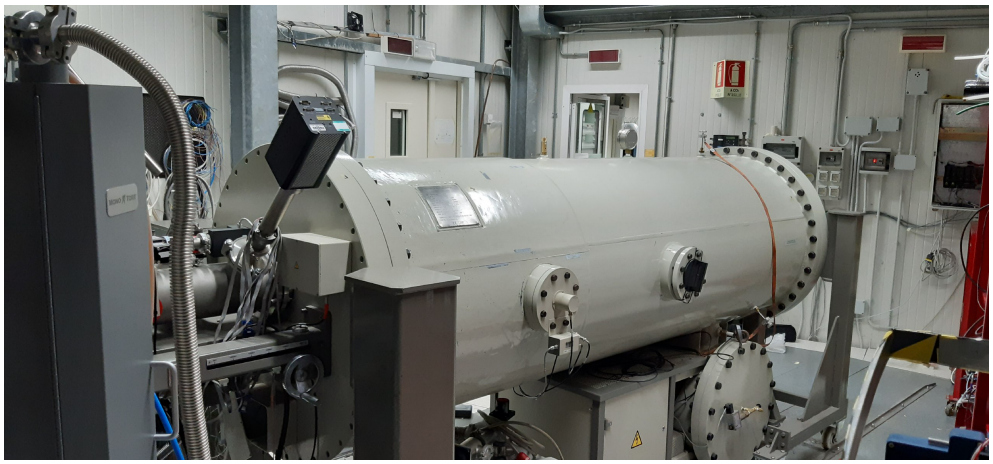

Figure 12: The LUNA 400kV accelerator tank.

decay product of ^{210}Pb, ^{210}Bi . The compromise found in the LUNA setup is a 25 cm lead shield (specifically chosen to have ^{210}Pb < 25Bq/kg), thicker than what possible on overground laboratories where the muon background causes activation in the shielding.

Another problem to cope with is the presence of radioactive radon gas in the air, this is typically dealt with enclosing the detector in an anti-radon box, kept airtight and flushed with nitrogen gas.

With these measures in place, the background of the LUNA detector was extensively studied either with Bismuth Germanate (BGO) scintillators, High Purity Germanium (HPGe) and silicon detectors and found to be unprecedentedly low [28, 29].

Typical background spectra for a shielded setup at LUNA are shown in Fig. 17 and discussed in section 2.4.2, the count rate obtainable for the most prominent lines is of only a few counts per hour.

2.2 THE 400 KV ACCELERATOR

Given that the cross sections involved in nuclear astrophysics are typically very low and the energy dependence is very steep (see eq. 8) the two most important features needed for an accelerator in nuclear astrophysics are high beam intensity and long time stability of the terminal high voltage (HV).

A 400 kV electrostatic accelerator, manufactured by High Voltage Engineering [30], is currently installed at the LUNA facility (Fig. 12). It is of Cockcroft-Walton design, enclosed in a pressurized chamber filled with a mixture of N_2 and CO_2 in order to avoid sparks between the various components. A radio-frequency ion source installed inside the chamber is capable of providing proton or alpha beams with an intensity as high as 500 μA on target. Using a 45 degrees magnet and a vertical steerer the ions are selected and focused, they can be delivered on one of the two beam lines, one for a solid target and one for a windowless gas target (see section 2.3).

The system in place has been calibrated with an accuracy of 0.3 keV and is capable of providing beam with an energy spread of about 100 eV and

long term stability of 5 eV/h for periods up to 4 weeks of continuous operation [30].

2.3 THE GAS TARGET SYSTEM

The measure of the $^{20}Ne(p,\gamma)^{21}Na$ reaction will take place using a gas target of the windowless type. The use of this type of targets is often unavoidable in nuclear astrophysics: solid targets should be formed typically using gaseous elements or from chemical compounds of these isotopes which degrade rapidly over time and usually suffer from uncertain stoichiometry.

Gas targets, on the other hand, offer a number of advantages over a solid target setup, most importantly the target stability over time is excellent, having the ability to sustain high intensity ion beams over a longer period of time. Another advantage of the gas targets is that typically they have a stronger isotopical purity and suffer less of beam induced background from contaminants. The downside is that the detection efficiency for each interaction point in the target chamber needs to be properly characterized and accounted for and this can make the analysis more difficult, as discussed in section 3.3.1.

The windowless solution, achieved through a differential pumping system [18], is typically preferred in the high current low beam energy regime of nuclear astrophysics. A window between the high vacuum of the beam line and the gas target chamber might introduce significant energy loss and straggling at these energies and would inevitably suffer from quick degradation if thin enough to mitigate this two problems.

In Fig. 13 a scheme of the LUNA gas target system is shown. In this setup, the gas is continuously pumped away through a three-stage pumping system. The pressure inside the chamber is typically on the order of a few mbar and drops of roughly three orders of magnitude thanks to two high-speed pumps Roots pump (2050 m^3/h, 500 m^3/h) in series and a first long, high impedance, water-cooled aperture (AP1 in Fig. 13). Following another aperture (AP2) the subsequent pumping stages can eliminate the remaining gas using three turbomolecular pumps. The system is connected to the beam line following another pumping stage (through AP3), typical pressure in the last two sections are $10^{-6} - 10^{-7}$ mbar.

Since the gas is lost over time, it needs to be continuously refilled inside the chamber using gas inlet valves controlled through a gauge system that measures the pressure inside the chamber.

For expensive gases, like isotopically enriched ones, the system is equipped with a recirculation system, in this case the exhaust of the 500 m^3/h Roots pump are sent through a purifier that removes nitrogen and oxygen contaminations and stored in a buffer volume (see [31] for details).

The reaction chamber employed will be the same one implemented in previous cross section studies on the $^{22}Ne(p,\gamma)^{23}Na$ reaction [18, 32, 33] and studied with the same type of gas. For this reason, the present work will heavily rely on the characterization done on that experiment.

At the end of the chamber, the beam is stopped and its intensity is measured using a beam calorimeter (Fig. 14). This is the typical approach used

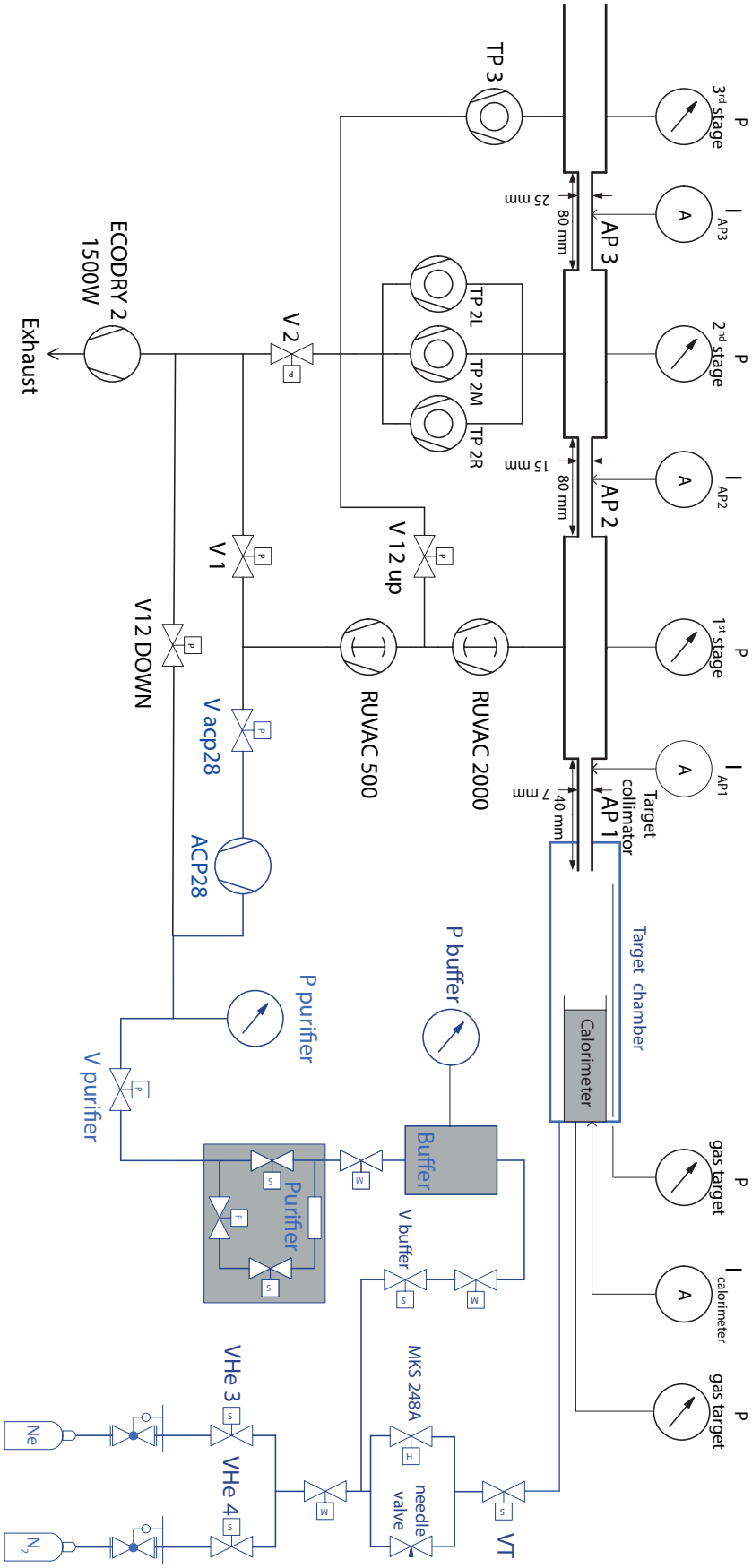

Figure 13: A scheme of the differential pumping system, taken from [18].

Figure 14: The calorimeter system installed at the end of the target chamber in February 2020. The hot side is on the top in the picture, the two copper tubing on the sides are connected to pressure gauges.

in gas target setups, as the production of secondary electrons by the interactions of the beam with the gas is an issue and the charge cannot be simply collected and integrated at beam stop.

Here a constant gradient of temperature is maintained using a control system. A resistor dissipates power via the joule effect on the hot side, which is exposed to the gas target, a chiller is employed on the outer side of the calorimeter to maintain a gradient of temperature. Once the accelerator is running and the hot side is exposed to the beam, less work is dissipated on the resistance to maintain a constant temperature gradient, this is directly proportional to the beam intensity. In order to operate this system, a calibration is mandatory and can be done evacuating the chamber and measuring the beam intensity in vacuum where the production of secondary electrons is negligible and charge can be properly integrated (see section 2.4.4).

2.4 EXPERIMENTAL SETUP

This section describes the conceptual design of the setup that will be used in the measurement as well as some consideration regarding its characterization made during the initial building phase of the apparatus in February 2020. Unfortunately, the ^{20}Ne campaign was suspended the following month because of the sanitary crisis. Considering the situation, the hope of this is work is now to give a proper description of the setup. The following chapter

will then be devoted to the study of Monte Carlo (MC) simulations of the setup and the development of a proper measure strategy.

2.4.1 Setup design

Because the reaction has a Q-value relatively low all the γ rays emitted by the ^{21}Na are expected in a region of the spectra dominated by environmental radioactivity. The campaign is expected to study, as first goal, the resonance at E_R= 366 keV. To achieve this goal, the γ-rays from the transitions Res. $\rightarrow$ 2425, Res. $\rightarrow$ 332 and Res. $\rightarrow$ g.s. will be measured.

The expected γ-rays emitted from the reaction are emitted with energies

$$E_\gamma = Q + \frac{m_p}{m_p + m_t} E_p - \Delta E_{rec} + \Delta E_{Dop}, \tag{19}$$

where E_p the projectile energy in the lab system and m_p and m_t are the masses of the projectile and the target.

ΔE_{rec} is the correction for the recoil energy of the compound nucleus of mass m_B:

$$\Delta E_{rec} = \frac{E_\gamma^2}{2 m_B c^2}, \tag{20}$$

negligible for the 2.8 Mev γ-ray. The last term in Eq. 19 is the correction for the Doppler shift for nucleus moving with velocity v:

$$\Delta E_{Dop} = \frac{v}{c} E_\gamma \cos\theta, \tag{21}$$

where θ is the angle between the beam line and the γ-ray detector. It is worth to note that, since the projectile might interact at any position inside the target chamber, both E_p and ΔE_{Dop} depends on the interaction position: the projectile loses energy as it travel through the gas and it might interact at different relative angles with respect to the detector.

For the reasons mentioned above the best solution are *High Purity Germanium* (HPGe) *detectors* because of their excellent resolution, low intrinsic background, and not-so-low efficiency with low energy γ-rays. Nonetheless the efficiency is still not very high for this kind of detectors and, given the energy range of the γ-rays expected, a setup properly shielded from the environmental radioactivity is required.

The campaign is planning to install the setup already used in the successful measurement of the ^{22}Ne$(p,\gamma)^{23}$Na (shown in Fig. 15) [18]. In this configuration two HPGe detectors are placed at different axial positions outside the reaction chamber.

During this measurement two lead collimators were placed in a 90° and 55° arrangement with respect to the detectors in order to mitigate possible angular distribution effect in the emitted γ-ray. This solution will not be followed in the construction of new setup, giving the two detectors a wider line of sight, as discussed in section 3.1.

The entire configuration is then shielded using ~25 cm of low radioactivity lead. Each detector will also be surrounded by a few centimeters of oxygen-free copper in order to shield the HPGe against the bremsstrahlung photons

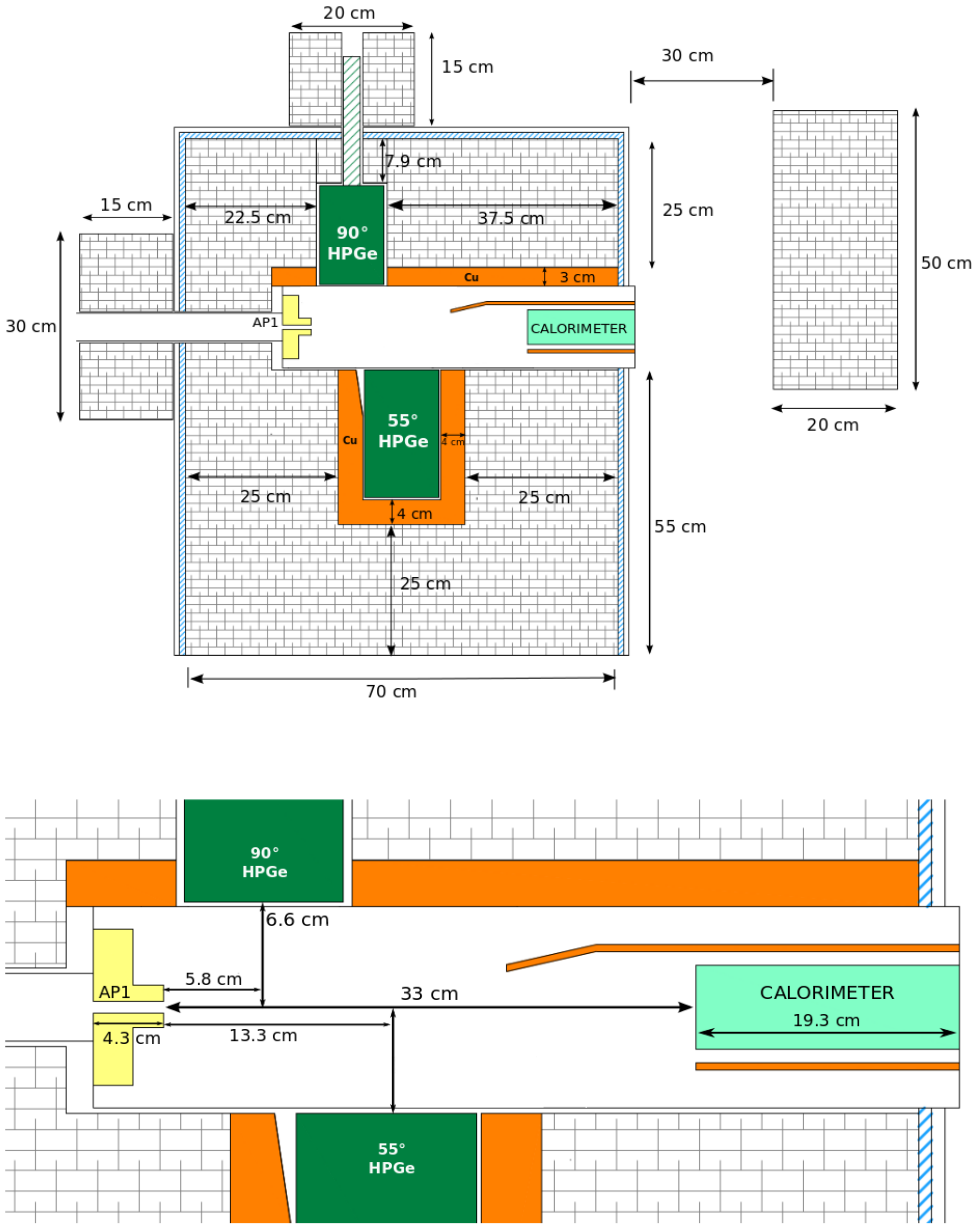

Figure 15: Drawing of the experimental setup used in the study of $^{22}Ne(p,\gamma)^{23}Na$. The same configuration will be used in the study of the $^{20}Ne(p,\gamma)^{21}Na$. Taken from [34].

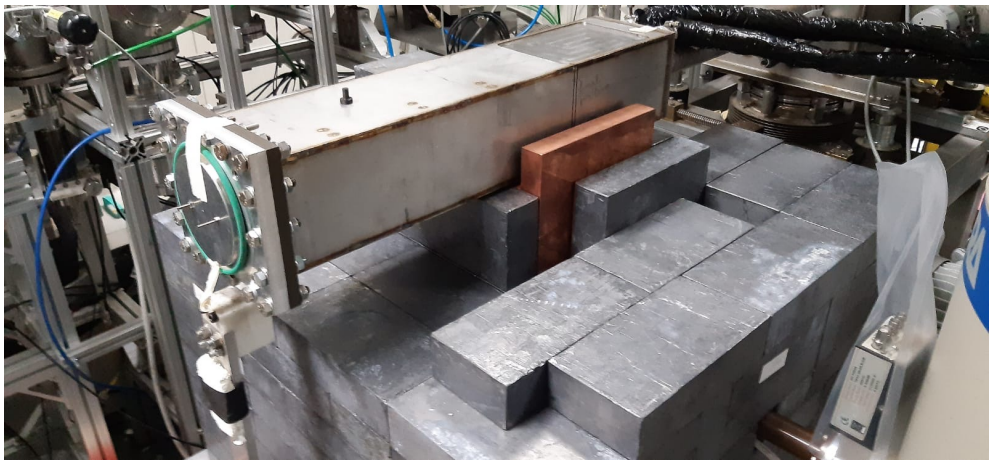

Figure 16: Status of the setup construction in February 2020, with the shielding partially built below the target chamber.

produced by the beta decay of ^{210}Bi, a radioactive isotope usually present in lead, daughter of ^{210}Pb.

The setup will be also enclosed in a Plexiglas anti-radon box, this container will be flooded with nitrogen gas to avoid the accumulation of radioactive radon gas inside the lead castle.

During the preliminary work of February 2020 the lower detector (GePD in the following), a Camberra low background HPGe detector with 130% relative efficiency powered by a SILENA 7716 high voltage power supply, was installed and the lead castle built up to the level of the chamber. Fig. 16 shows a photo of the status of the setup.

This configuration was used to take a few preliminary spectra of background, thoroughly.

2.4.2 Environmental background

The described setup configuration, already extensively characterized in [34], is expected to reduce the environmental background by about three orders of magnitude. In Fig. 17 a spectrum of the background obtained during this intermediate phase of the construction is shown. All the visible lines are given by the known transitions from the aforementioned radioisotopes.

This spectrum is compared with a previous one taken in October 2015 (same final detector configuration) with the setup fully shielded. Given this comparison, a reduction of at least another order of magnitude is expected for the final setup with counting rates in the regions of interest of about 10^{-3}-10^{-4} counts/s. The measured count rates in the region of interest of the experiment are reported in Tab. 2.

2.4.3 Beam-induced background

A particular attention will be devoted to the effect of beam induced background. In example, the chamber will be filled during the measurement with neon gas isotopically enriched in ^{20}Ne, up to 99.99%, in order to sup-

Transition	E_γ (keV)	Present setup (half shielding) (counts/s)	Setup 2015 (counts/s)
$332 \rightarrow gs$	332	2.66(2)	0.0098(4)
$res \rightarrow 2425$	373	1.99(2)	0.0062(3)
$2425 \rightarrow gs$	2425	0.026(2)	0.000 03(2)
$res \rightarrow 332$	2466	0.018(3)	0.000 02(2)
$res \rightarrow gs$	2797	0.0002(2)	-

Table 2: Environmental background counting rates in the regions of interest of the transitions for the 366 keV resonance in the $^{20}Ne(p,\gamma)^{21}Na$ reaction.

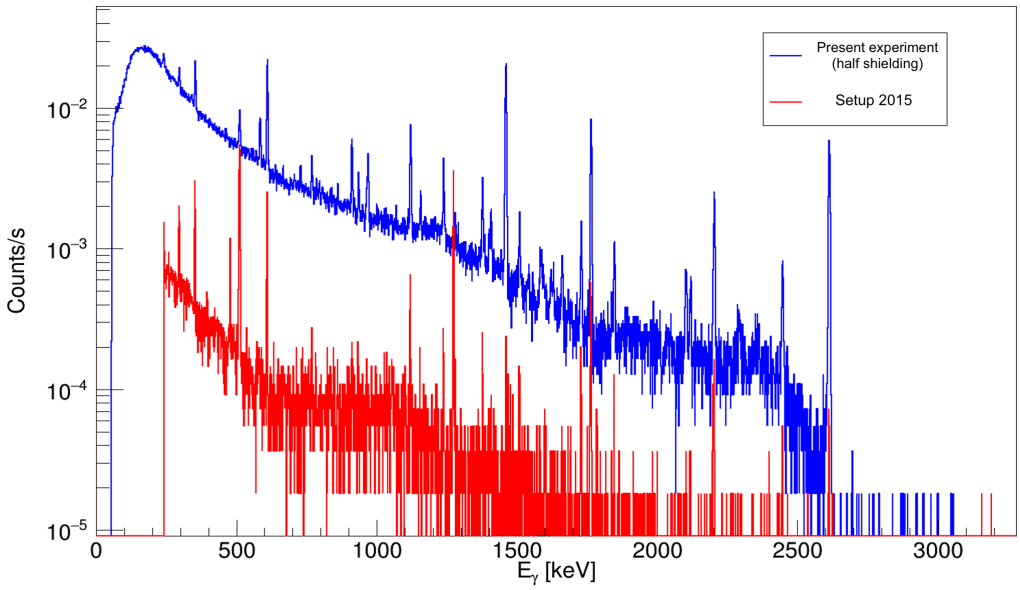

Figure 17: Laboratory background run taken with the HPGe detector positioned below the chamber. Blue spectrum is the laboratory background taken in February 2020 (setup not completely shielded) while the red one is the laboratory background taken in October 2015 (setup completely shielded).

press any resonant reaction from proton capture on ^{22}Ne (10% abundance in natural neon gas). Other common sources of beam-induced background includes low Z elements like deuterium, boron, carbon, oxygen, and fluorine. These contaminants can also be found on the surfaces exposed to the beam, in particular on the copper collimator and the calorimeter.

One of the main contaminants found in the spectra is fluorine. The reaction $^{19}F(p,\alpha\gamma)^{16}O$ has a high cross section below 400 keV and a resonance can be found at $E_p = 340$ keV. In fig. 18 a spectrum acquired during the characterization of the setup is shown. Here the calorimeter was installed for an initial test with the beam at $E_p = 341$ keV just above the fluorine resonance with the chamber evacuated. Signs of fluorine are clearly present around 5-6 MeV. Similar degrees of contamination were also found in another run where the beam was focused on the collimator of the target chamber.

Another source of contamination visible in the spectra is due to the reaction $^{12}C(p,\gamma)^{13}N$ that originates from the hydrocarbon absorbed into the surfaces exposed to the beam.

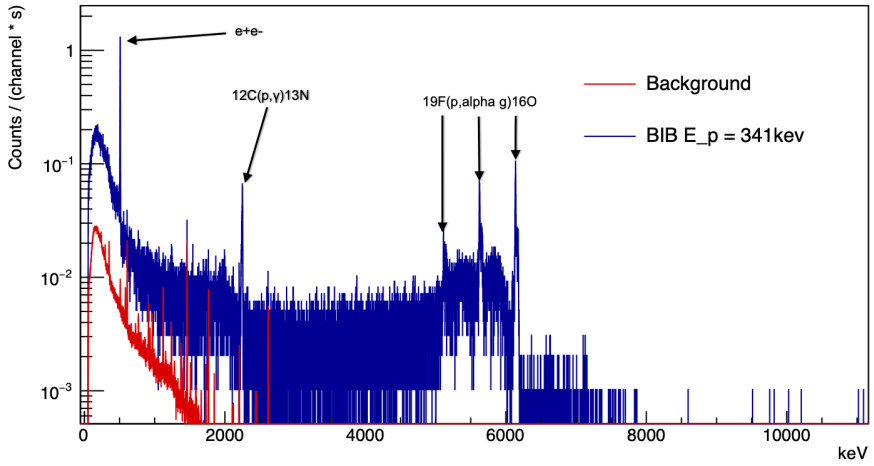

Figure 18: Beam-Induced background obtained during a preliminary test with beam at the energy of $^{19}F(p,\alpha\gamma)^{16}O$ resonance, compared to the background spectra obtained with half shielding built.

One way to reduce this type of contamination is cleaning very well the surfaces where the beam interacts. Otherwise, the reactions involved in this effect are very well known and can be mitigated (i. e. acquiring blank spectra).

2.4.4 Calorimeter calibration

Inside the reaction chamber the beam stops on a copper calorimeter attached to the end flange. As discussed in section 2.3 this device is used to measure the beam intensity in a context where is not possible to integrate the beam current directly.

This device is composed of a hot side exposed to the beam and kept at constant temperature of 70° by resistors and cold side kept at −3° by the cooling liquid provided by a chiller. Several PT100 sensors are used to measure the temperature of the hot side, these values are logged and used as feedback to give current to the resistors that dissipate energy on the hot side. Given W_0, the power dissipated with no current, the beam intensity can be calculated as

$$I = \frac{W_0 - W}{E_p - \Delta E} \tag{22}$$

where W is the power delivered by the resistors in presence of a beam, E_p the beam energy entering the chamber, and ΔE the energy lost through the gas.

The power measured by the calorimeter must be calibrated. This was done evacuating the chamber and measuring simultaneously the beam current using the calorimeter and the chamber as a Faraday cup. With simultaneous measurement of both the calorimetric power and the electrical power using the integrated current, a calibration line can be drawn.

During the last week of February 2020 a fast calibration has been performed after cleaning the target chamber. During the measurements, the

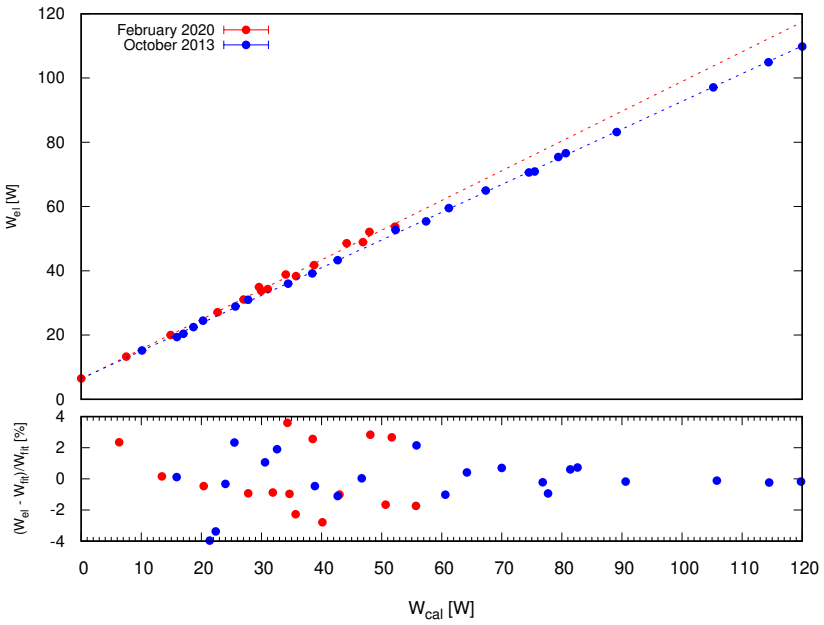

Figure 19: Calorimeter calibration February. 2020. Comparison of calibration taken in the previous campaign, October 2013.

calorimeter and the target chamber are electrically insulated from the upstream part by a 10 mm thick Teflon disk. These two pieces are connected together to form a Faraday cup. Several runs have been performed varying the proton energy from 50 keV to 380 keV. A current integrator unit, attached to NIM counter, was used to measure the total charge reaching the calorimeter and the chamber.

The calorimetric measurement of the power delivered by the beam is given by

$$W_{cal} = W_0 - W_{beam} \tag{23}$$

where W_0 is the average value of the zero power acquired before and after each run to check its stability, while W_{beam} is the power delivered when the beam is on. The calorimetric electric power is calculated for each run as:

$$W_{el} = \frac{E_{beam} I_{target}}{q_e} \tag{24}$$

The resulting calibration is shown in Fig. 19 and compared to older measurements.

The calorimeter calibration function obtained shows the trend of W_{el} as a function of W_{cal}:

$$W_{el} = mW_{cal} + q \tag{25}$$

where

$$m = 0.98 \pm 0.02, \qquad q = 0.1 \pm 0.6W \tag{26}$$

.

A linear function fit all the data proving that the calibration remains constant in time. The residual plot shows that, for almost all data points, the deviation from the fitting function is less than 3% (average discrepancy of 1.8%).

The slope of the calibration function, being closer but less than unity, is mainly a consequence of parasitic currents in the system. Furthermore an important contribution comes from the different heat flow between the beam current heating, that is more localized, and the heating generated by the resistors, that is more spread out. The slope of the function showed in Fig. 19 for the calibration of the 2020 calorimeter is actually closer to unity than the showed calibration for the 2013 campaign thanks to an improved design of the calorimeter discussed in [31], providing more uniform heating at beam stop.

3 ANALYSIS

In this chapter, the study of the setup and its preliminary characterization using Monte Carlo simulations are reported. The experimental configuration expected for the study of the reaction is tuned in the Monte Carlo using both the experimental data from the 2015 campaign and the few 2020 measurements available. A study of the 366 keV resonance is then performed. This allows us to choose the best condition for the measurement, constrain the expected count rate and other effects such as beam energy straggling inside the gas target.

3.1 DETECTION EFFICIENCY CALIBRATION

In an extended gas target, the beam can interact at any position along the beam axis. As a consequence of this fact, the photons can be emitted at different positions along the beam line, thus at different distances from the detectors. For instance, our configuration is shown in Fig. 20. Here we will define z as the beam line axis. The entrance of the chamber (end of the collimator) refers to position $z = 0$. The reaction can take place at any point along the beam line. By changing the distance from the detectors also the subtended angle of the emitted photon with respect to the beam line is modified.

The photons emitted at different angles are firstly affected by different amounts of Doppler shift. For example, the correction from Eq. 21 for a 2.8 MeV photon varies from $+3.7$ keV at 20° to -3.7 keV at 160°, this correction is negligible for photons emitted at 90°, above one of the two detectors. Another crucial aspect is that the detection efficiency depends on the solid angle covered by the detector, and, as a consequence, from the position where the reaction takes place.

The *absolute full-energy peak efficiency* is by definition the ratio between the measured peak area and the total number of gamma emitted by a radioactive source over the whole solid angle:

$$\eta(E) = \frac{N(E)}{A \cdot t \cdot Br}, \tag{27}$$

where $N(E)$ is the peak area, A the source activity, t the time of measure, and Br the branching ratio of the transition. This quantity depends on the position of the emission inside the target chamber and the gamma energy. It needs to be measured over the widest possible range of energies and positions inside the target chamber.

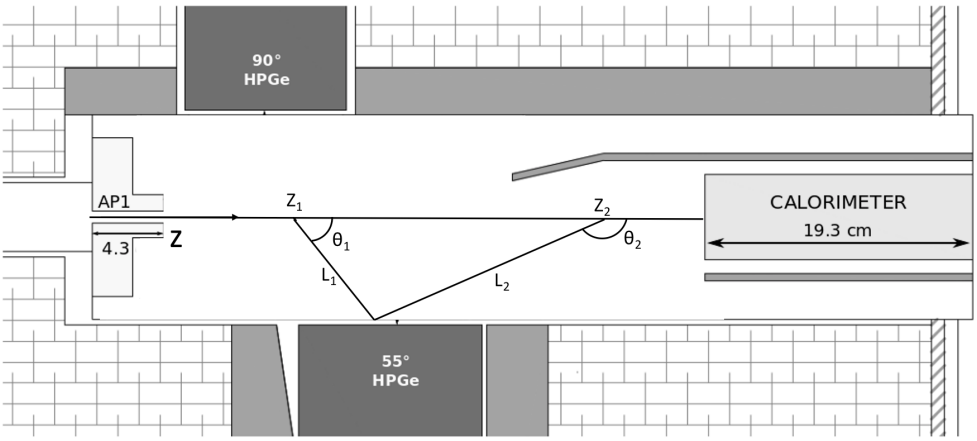

Figure 20: The reaction can take place at any position along the beam line, changing, depending of the position, the distance from the detectors (and therefore the detection efficiency) and the angles θ, that influences the Doppler shift of the emitted photons.

3.1.1 Preliminary source calibration at LNGS

In February 2020 it was possible to take a preliminary measurement of the efficiency of the setup. For this purpose a movable holder fixed at the back flange of the chamber allows to place point-like sources at different distances from the entrance collimator (Fig. 21). The holder consists of a PVC frame designed to fix in place the disk containing the radioactive sample at a determined position along the beam and in such a way to keep its shadow negligible. A rectangular rod takes the holder in place and is fixed with a flange at the back of the chamber.

Typically this configuration allows the calibration of the detectors in the low energy range using several radioactive sources like ^{60}Co,^{137}Cs, and ^{88}Y. During the preliminary phase of the experiment it was only possible to take the efficiency measurement for the lower detector using a ^{60}Co placed at several different positions inside the chamber along the beam line.

The efficiency profile for the two peaks (E_γ = 1173.23 keV, 1332.49 keV) of the ^{60}Co source is obtained for the installed lower detector. This result is used to better constraint the geometry inside the GEANT code. Regarding the upper detector (referred to as GeDD in the following), analogous measurements, obtained during ^{22}Ne(p,γ) LUNA campaign (same final expected configuration), where employed to design the simulations.

3.1.2 Monte Carlo simulation

The experimental setup has been implemented in GEANT-3 [35] in order to simulate the detection efficiency of the chosen geometry and later on the reaction, in particular the resonant capture.

This older version of GEANT, written in FORTRAN, was chosen instead of the newer version because the custom code is already thoroughly tested and validated in several past LUNA campaigns [31, 36, 37] and various effects present for the gas target setup, such as beam energy straggling, are

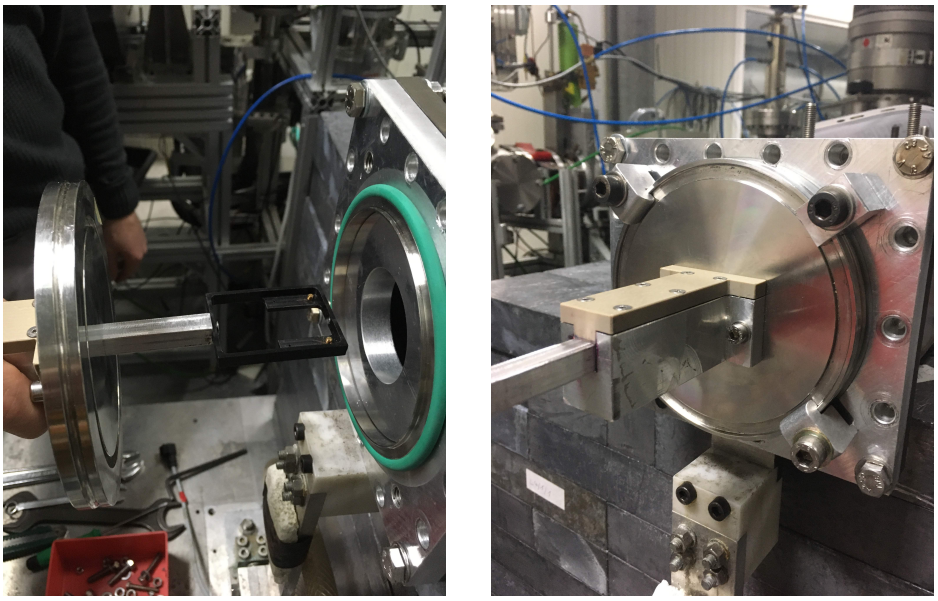

(a) Source holder **(b)** Holder mounted on the end flange

Figure 21: The movable holder for the calibration sources shown on the left, on the right mounted on the end flange of the chamber.

implemented, along with the code necessary to simulate reactions given a set of parameters (e. g. direct capture, resonance width).

The geometry of the chamber, the collimator, the surrounding materials, and the detector was measured and implemented inside the code (in Fig. 22 a side view from GEANT is shown).

A preliminary tuning of the geometry was necessary. In order to do this, a ^{60}Co source is simulated inside the chamber at fixed positions along the beam line. Then the spectra obtained with the Monte Carlo are normalized and compared to the experimental ones (see Fig. 23). The efficiency for a photo-peak for each simulated run is obtained as the ratio between the area of the peak in the MC spectrum and the total number of events simulated in the run, $\eta_{MC} = N/N_{tot}$. This estimate was made for the two detectors and compared to experimental efficiency profiles, the one acquired in February was used for the lower detector. Since the upper HPGe is not mounted yet, the efficiency profile was tuned using data from a calibration run of the detector taken on one of the previous LUNA campaigns with the same experimental configuration [32].

The main feature to adjust to reproduce a good agreement of the experimental and Monte Carlo data are:

- The distances of the detectors from the beam axis.
- The dead layers thickness of the detectors (effectively acting on the active volumes).
- Distances between Pb shielding and the steel reaction chamber.
- Distances between the detectors' casings and the steel reaction chamber.

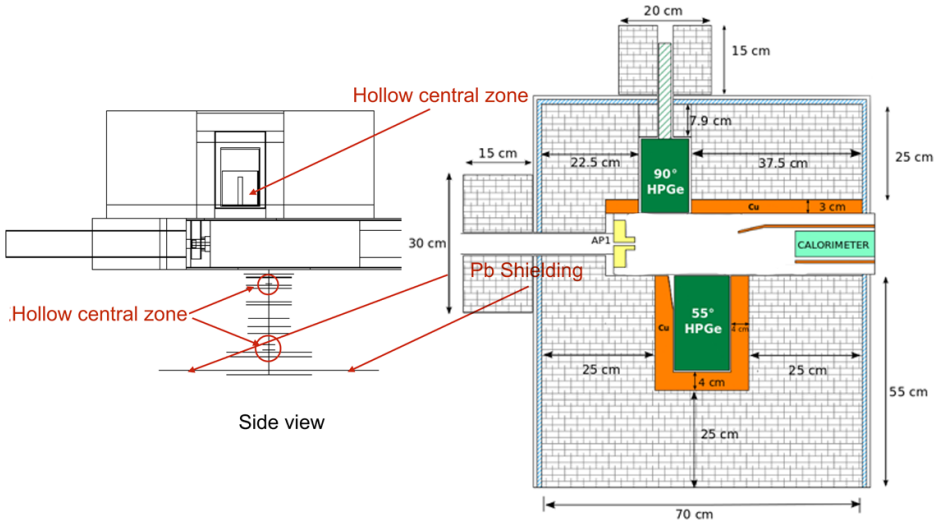

Figure 22: Side view of the setup geometry simulated with the GEANT-3 code, with the sketch of the chamber on the left for reference. The lower detector geometry is correctly implemented despite not showing up correctly in the graphical visualization reported here.

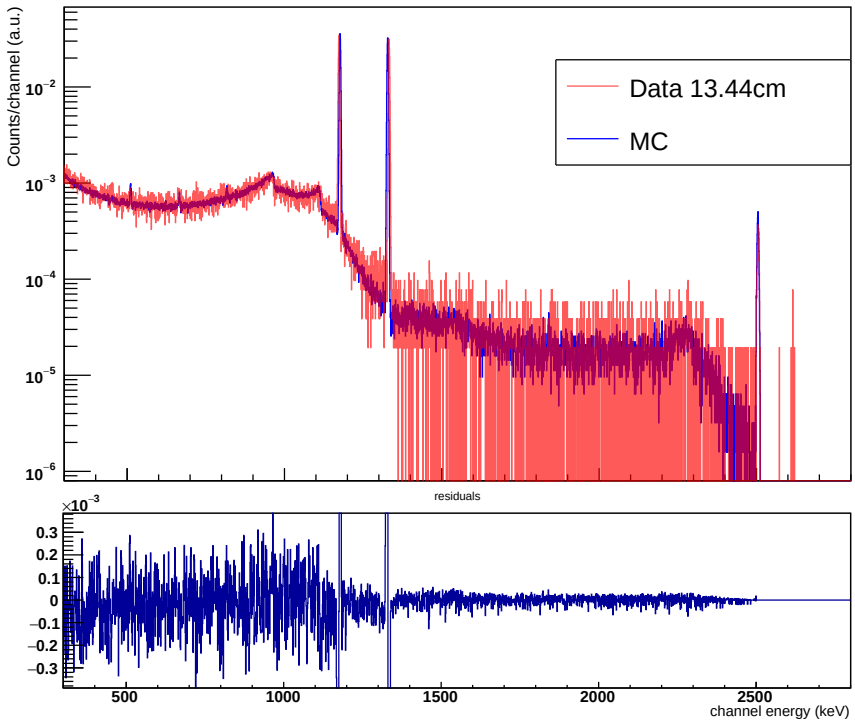

Figure 23: Comparison between an experimental calibration run using ^{60}Co source and MC spectra for the lower HPGe detector, no significant distortion is present.

These parameters were adjusted, inside reasonable ranges, considering also the past experience of the LUNA collaboration working with the two HPGe taken into account.

The final result of this calibration is shown in Fig. 24. For the lower detector (GePD) the discrepancies between Monte Carlo and experimental data is less than 2%.

In order to give the best possible description of the upper detector (GeDD), it was compared to data from the experimental ^{22}Ne phase of the LUNA experiment. The final implemented geometry needed significant tuning with respect to the one taken from technical sheets from the manufacture. In fact, over time, the active region was significantly reduced from nominal values as a result of past maintenance undergone by the detector. Finally, the agreement with the past calibrations at maximum efficiency is ~8%. Since it was not possible to have more recent experimental data, this agreement is good enough for our purposes and can be improved once the detector will be put in place.

In order to have a complete description of the efficiency $\eta(E, z)$ as a function the distance from the collimator z and the energy E for both detectors, several monoenergetical sources are simulated inside the ranges 1 cm$\leqslant z \leqslant$25 cm and 200 keV$\leqslant E \leqslant$3200 keV. The data obtained from this Monte Carlo run at fixed positions have been fitted with second order polynomials in the double logarithmic plane:

$$\eta(E, z) = \exp\Big(a(z) + b(z)\ln(E) + c(z)\ln^2(E)\Big). \tag{28}$$

An example of the calibration fit is shown in Fig. 25.

The parameters $a(z)$, $b(z)$ and $c(z)$ are then fitted with third and fourth degree polynomial in order to obtain a full parametrization of the efficiency. The results are shown in Fig. 26.

3.2 ENERGY LOSS AND STRAGGLING

Passing through matter, charged ions lose energy primarily by means of inelastic collision with the absorber nuclei. At each collision the ion loses a small fraction of its energy. The process is then statistical in nature and makes sense to introduce the energy loss per unit path length. This rate is referred to as *linear stopping power*:

$$\epsilon_{lin}(E) = -\frac{dE}{dx}, \tag{29}$$

where dE is the energy lost in penetrating a distance dx in the absorber.

It is usually more useful to refer to *mass stopping power* $\epsilon(E)$, defined as energy loss per unit areal density ρ,

$$\epsilon(E) = -\frac{dE}{d\rho} = -\frac{1}{N}\frac{dE}{dx}, \tag{30}$$

where N is the number density (atoms per cm^3) of the target material. The theoretical calculation of the stopping power is not an easy task. The Bethe-

(a) Lower Detector (GePD)

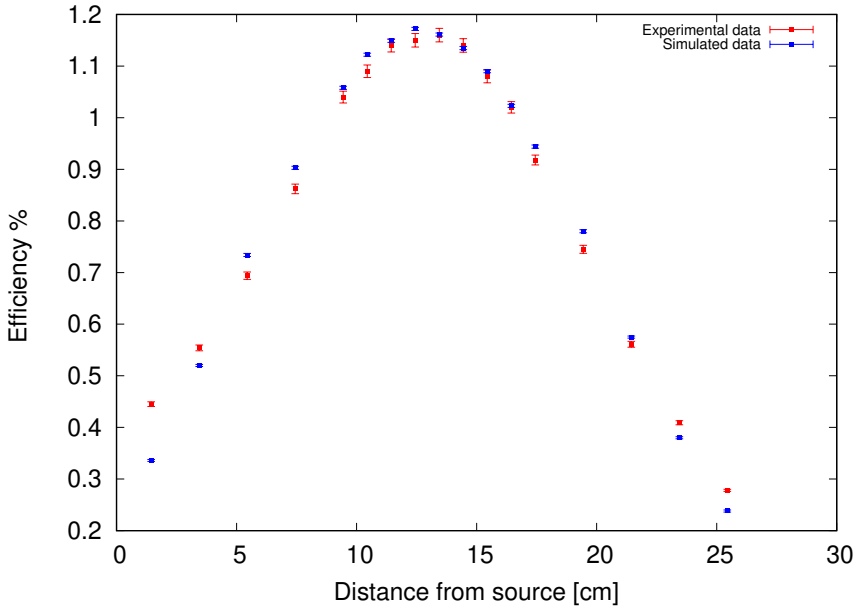

(b) Upper detector (GeDD)

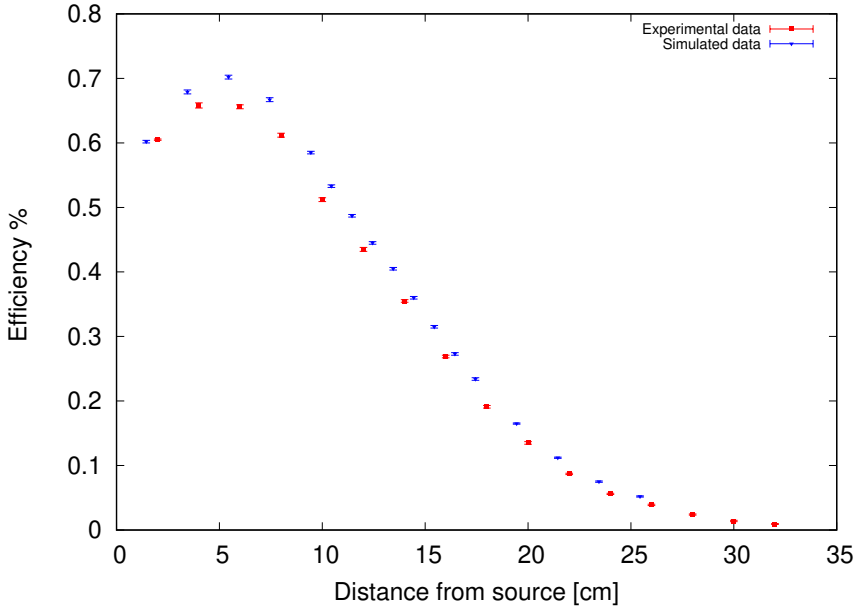

Figure 24: Efficiency profile for the 1333 keV photopeak of ^{60}Co, comparison between the MC and the experimental setup.

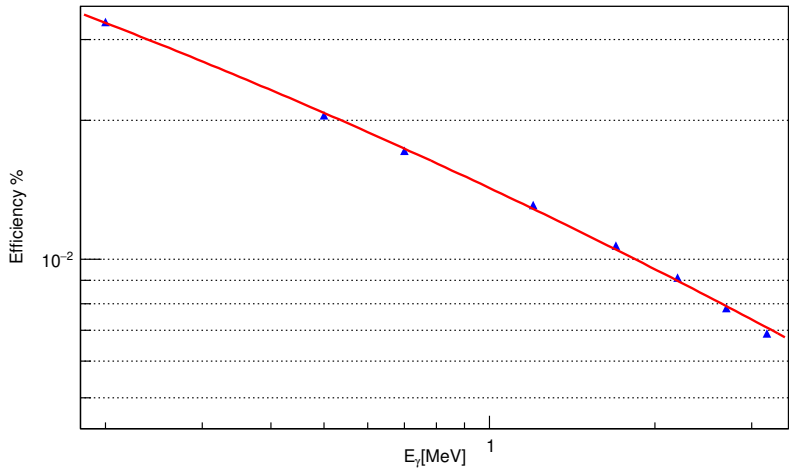

Figure 25: Example efficiency calibration of the lower detector (GePD) for the Monte Carlo. Here monoenergetical sources are simulated at distance from the collimator $z = 13$ cm, between 200 keV and 3 MeV. The fitted function Eq. 28 has parameters $a = -4.250 \pm 0.001$, $b = -0.564 \pm 0.001$, $c = -0.032 \pm 0.001$.

Block formula describes reasonably well the energy loss for high projectile energies (> 0.6 MeV/u):

$$-\frac{dE}{dx} = \frac{4\pi^4 z^2}{m_e v^2} NB \tag{31}$$

where

$$B = Z\left[\ln\left(\frac{2m_e v^2}{I}\right) - \ln\left(1 - \frac{v^2}{c^2}\right) - \frac{v^2}{c^2}\right], \tag{32}$$

that describes the theoretical electronic stopping power for a projectile of charge z and velocity v, passing through a medium of atomic number Z. I is the empirically determined ionization potential and m_e is the electron rest mass. The B function in Eq. 31 varies smoothly with respect to the energy and the stopping power is approximately inversely proportional to E (since $E \propto 1/v^2$).

If the projectile has energy approximately lower than 30 keV/u the nuclear component of the stopping power has to be taken into account. In this condition Eq. 31 no longer holds and the energy loss must often be determined with experimental measurements.

It is then also usual to define the *effective stopping power* that takes into account solid or gaseous target where the nucleus of interest takes part in a chemical compound:

$$\epsilon_{eff} = \epsilon_a + \sum_i \frac{N_i}{N_a}\epsilon_i \tag{33}$$

where N_a is the active nucleus of interest, N_i refers to the inactive nuclei in the compound each of them with effective stopping power ϵ_i, for example using natural neon ^{21}Ne and ^{22}Ne needs to be accounted.

A monoenergetic ion beam when passing through a medium will not only lose energy as described but also increase its spread. This effect, known as *energy straggling*, is caused by statistical fluctuation in the number of in-

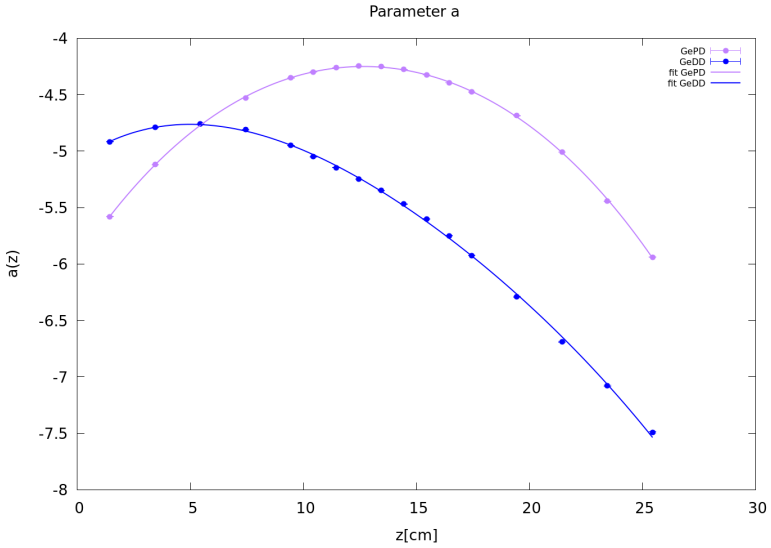

(a) Parameter $a(z)$

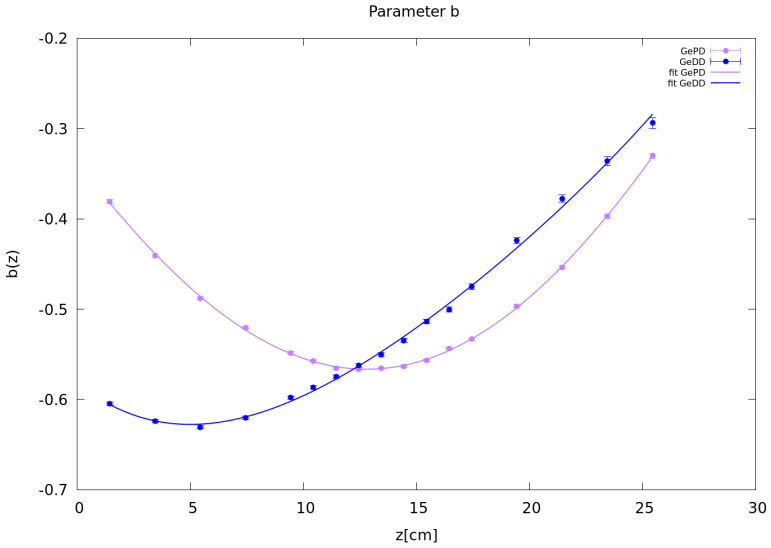

(b) Parameter $b(z)$

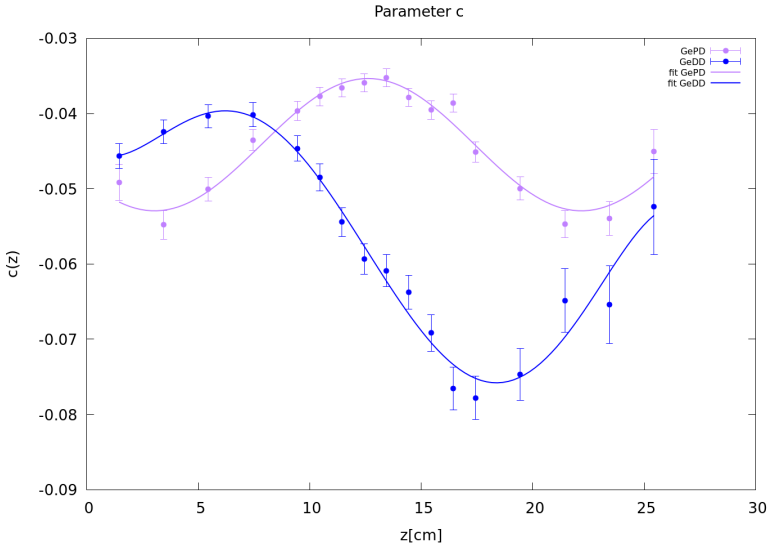

(c) Parameter $c(z)$

Figure 26: Coefficients of the efficiency parametrization (Eq. 28) fitted as a function of the distance from the chamber collimator (GePD is the lower detector and GeDD the upper detector).

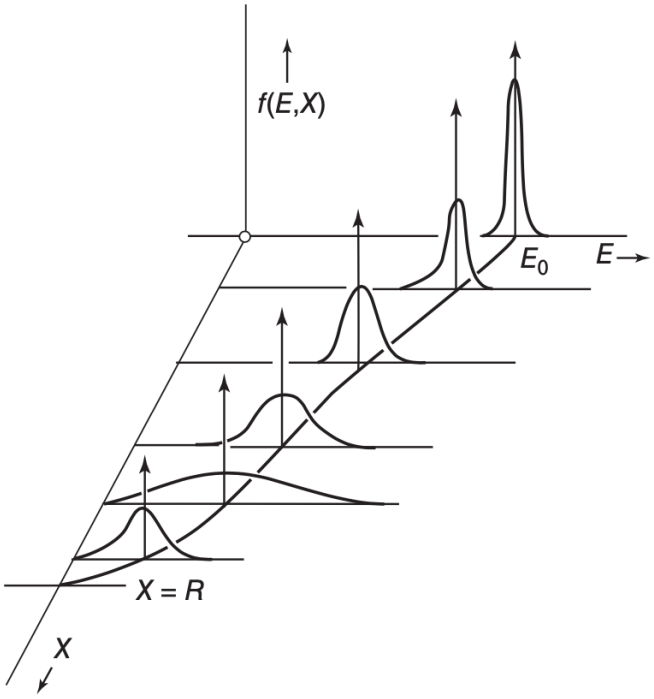

Figure 27: Representation of the effect of the energy straggling on an initially narrow beam of charged particles. Taken from [38]

teractions of the projectile inside the target (Fig. 27). A useful relation to characterize the straggling was derived by Bohr [39]. The width of the energy spread, well described by a Gaussian p.d.f, is approximated for non-relativistic heavy charged particles having standard deviation

$$\sigma_{\text{stragg}} = \sqrt{4\pi e^4 Z_p^2 Z_t N d}, \tag{34}$$

where Z_p and Z_t are the atomic numbers of the projectile and target and d is the crossed distance inside the target. This formula yields for a proton beam inside a gas target of ^{22}Ne at 2 mbar a σ_{stragg} of about 1.1 keV.

If a resonant reaction is considered, beam energy straggling affects the position in which the resonance takes place. A narrow resonance would be populated in a very well defined position inside the target if no straggling is present. By taking into account this effect, the resonance is populated in a larger slide inside the target.

The effects of energy loss and beam energy straggling are parametrized using the software SRIM (Stopping and Range of Ions in Solids) [40]. These effects are then implemented inside the GEANT-3 code.

Studying the resonance, the parametrization extrapolated using SRIM is

$$\sigma_{\text{stragg}} = 0.366 \cdot \Delta E^{0.554}, \tag{35}$$

where $\Delta E = E_{\text{beam}} - E_{\text{res,LAB}}$. This formula obtained empirically can be compared with Eq. 34 using the relation

$$\Delta E = \left(\frac{1}{N}\frac{dE}{dx}\right)_{E_{\text{beam}}} N d, \tag{36}$$

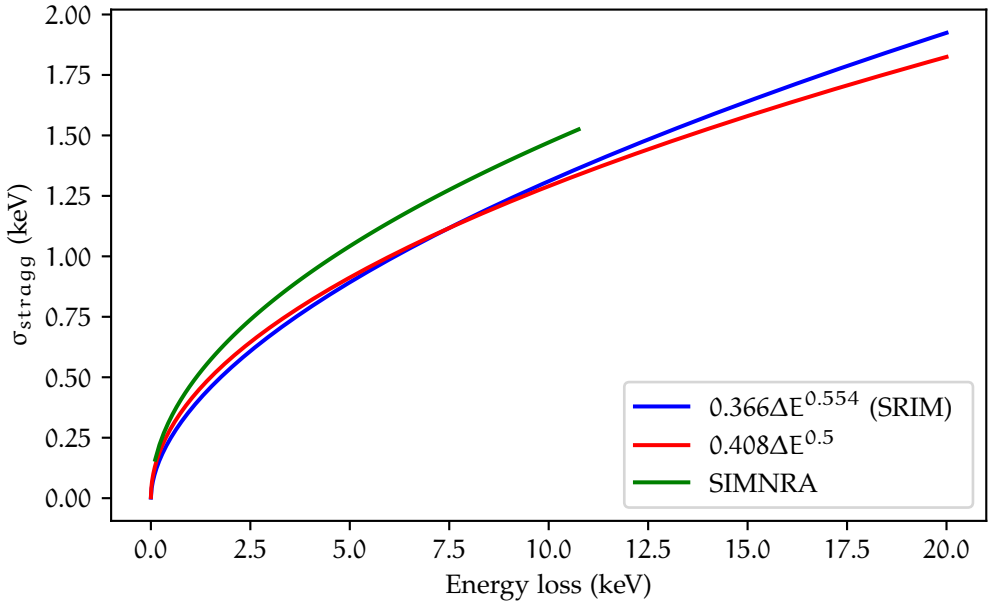

Figure 28: Comparison between the straggling parametrization obtained with SRIM (in blue), the one obtained with Eq. 34 (in red) and the correction to Bohr approximation given by SIMNRA [41].

that yields the formula (cf. Iliadis [2] pp.323)

$$\sigma_{\text{stragg}} = 4.08 \times 10^{-10} \sqrt{\frac{Z_p Z_t^2}{\epsilon} \Delta E} = 0.408 \sqrt{\Delta E} \quad \text{(keV)}. \tag{37}$$

Fig. 28 shows a comparison between the two parametrizations of the straggling obtained as well as the correction to Bohr's approximation as reported in the user manual [42] of the software SIMNRA [41]. This last approximation varies significantly from the other two estimates. Section 3.5 will explore the possibility of independently measure the straggling using the two HPGe included in the setup.

3.3 YIELD FROM A RESONANT REACTION

As discussed on section 1.1.1, the resonance strength $\omega\gamma$ is the main quantity that allows us to calculate the reaction rate in the presence of a narrow resonance (Eqs. 14,15).

The measured quantity in a nuclear physics experiment is the *reaction yield*:

$$Y \equiv \frac{\text{number of reactions}}{\text{number of incident particles}}, \tag{38}$$

This quantity is given experimentally by

$$Y = \frac{N}{N_b \eta B W}, \tag{39}$$

where N is the total number of detected particles or photons, η the detection efficiency, B the branching ratio, W the angular correlation for a specific transition and N_b is the total number of incident projectiles (i.e. Q/e, the total integrated current divided by the elementary charge for a proton beam).

Consider now a thin slice of target material dx, the infinitesimal yield from this slice is

$$dY = \sigma N dx, \tag{40}$$

the total yield is obtained integrating over all target slices

$$Y(E_0) = \int \sigma(x) N(x) dx = \int \sigma(E) N(x) \frac{dx}{dE} dE, \tag{41}$$

using the definition of stopping power (Eq. 30) the yield becomes

$$Y(E_0) = \int_{E_0 - \Delta E}^{E_0} \frac{\sigma(E)}{\epsilon(E)} dE \tag{42}$$

where ΔE is the total energy lost inside the target.

If a resonance is present between E_0 and $E_0 - \Delta E$ and gives a significant contribution to the total yield the cross section of the Briet-Wigner (Eq. 13) can be substituted into Eq. 42:

$$Y(E_0) = \frac{\lambda^2}{2\pi} \frac{m_p + m_t}{m_t} \frac{\omega\gamma}{\epsilon_r} \left[\arctan\left(\frac{E_0 - E_r}{\Gamma/2} \right) - \arctan\left(\frac{E_0 - E_r - \Delta E}{\Gamma/2} \right) \right]. \tag{43}$$

If the resonance width is small compared to the target thickness ($\Gamma \ll \Delta E$) the maximum yield becomes

$$Y_{max} = \frac{\lambda^2}{2} \frac{m_p + m_t}{m_t} \frac{\omega\gamma}{\epsilon_r}, \tag{44}$$

This equation can be compared to Eq. 39 in order to obtain the resonance strength in the thick target approximation.

In a more realistic approximation, the effects of beam energy resolution and energy straggling needs to be taken into account in the determination of the yield. A complete treatment including these effects (given by [43]) leads to the more general expression

$$Y(E_0) = \int_{E_0 - \Delta E}^{E_0} dE' \int_{E_i = 0}^{\infty} dE_i \int_{E=0}^{E_i} \frac{\sigma(E)}{\epsilon(E)} g(E_0, E_i) f(E_i, E, E') dE \tag{45}$$

where $g(E_0, E_i)$ describes the beam energy distribution and $f(E_i, E, E')$ is the probability distribution related to energy straggling.

3.3.1 Yield correction for the LUNA gas target

The physical displacement of the detectors in relation to the gas target also plays an important role in the particular setup considered in this thesis, as already discussed in [44].

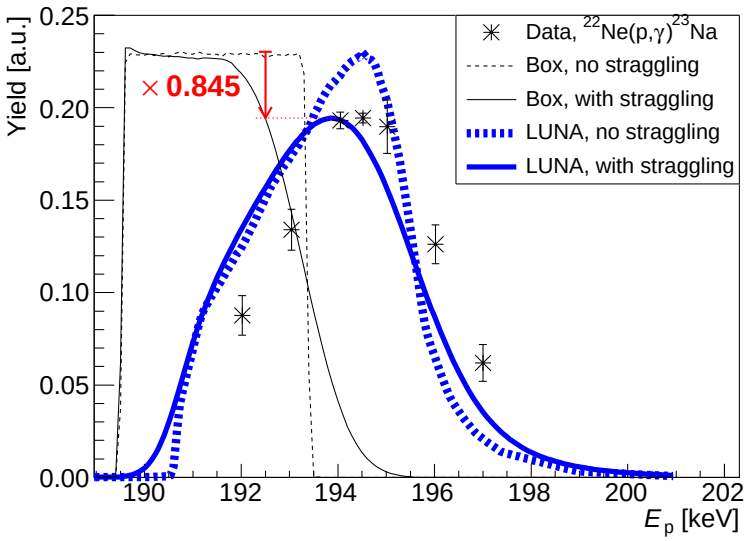

Figure 29: The effect of beam energy straggling on experimental yield for a resonance of the $^{22}Ne(p,\gamma)^{23}Na$, obtained with the same setup as in this thesis, taken from [44].

Resonances are typically extracted for thick target reversing Eq. 44 as

$$\omega\gamma = \frac{2Y_{max}\epsilon_r}{\lambda^2}\frac{m_t}{m_p + m_t}, \tag{46}$$

while the thick target condition is typically satisfied for the considered resonance as $\Delta E \gg \Gamma = \Gamma_p + \Gamma_\gamma$. The physical spread of the beam and the uneven target density found for windowless gas target system, shown in Fig. 15, contributes significantly. In this context, the resonance scan never reach a plateau and it is possible to obtain the experimental yield profile (i. e. the product between the yield as described above and the efficiency $Y \times \eta$) integrating

$$Y(E_p) = \int_{\tilde{x}=0}^{\tilde{x}=\tilde{x}_{max}} d\tilde{x} \int_{E=E_p}^{E=0} \sigma_{BW}(E) f_{beam}(E, E^{mean}_{slowed}(\tilde{x})) n(\tilde{x}) \eta(\tilde{x}) dE \tag{47}$$

where $f_{beam}(E, E^{mean}_{slowed}(\tilde{x}))$ is the energy distribution of the slowed beam (almost Gaussian) as simulated with SRIM:

$$f_{beam}(E, E^{mean}_{slowed}) = \exp\left[-\frac{(E - E^{mean}_{slowed})^2}{2\sigma^2_{stragg}(E^{mean}_{slowed}) + 2\sigma^2_{beam}}\right]. \tag{48}$$

This approach, discussed in [44], led to the derivation of a correction on the resonance strength obtained using Eq. 46 (see Fig. 29).

In the case of the simulation implemented for the study of the $^{20}Ne(p,\gamma)^{21}Na$, the effects of beam energy straggling are implemented into the simulation. The events are generated inside the chamber with the corrected distribution. With this approach it is possible to extract the resonance strength comparing Eq. 39 and Eq. 44. The efficiency is derived from the simulation performed in the same experimental condition, using $\eta = N_{count}/N$, where N_{count} is the area of the peak and N the total number of events simulated at the resonance.

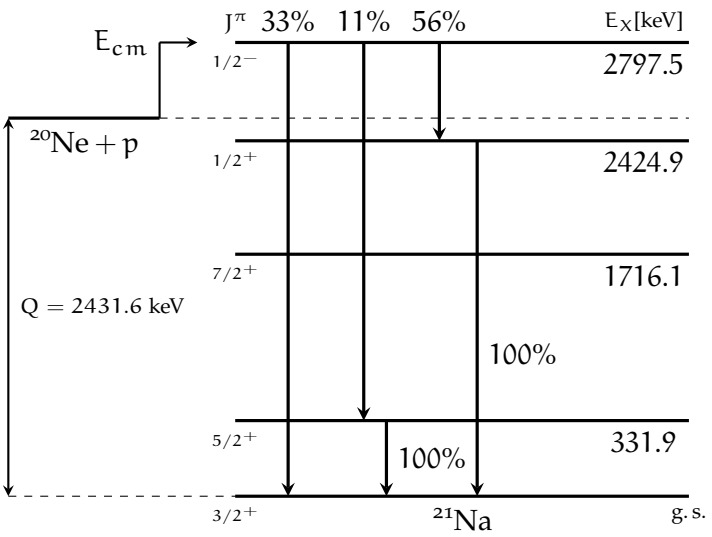

Figure 30: Decay scheme for $E_R^{lab} = 384.5$ keV resonance, with branching rates for the transitions taken from [22].

3.4 366 KEV RESONANCE

As already seen in chapter 1, the $^{20}Ne(p,\gamma)^{21}Na$ has a narrow resonance in the energy range of the LUNA-400 accelerator. This resonance is located at $E_R^{CM} = 366$ keV, or equivalently $E_R^{lab} = 384.5$ keV, and energetically available in the high temperature environments of oxygen-neon novae (0.1-0.45 GK) [45]. It corresponds to the 2798 keV excited state of ^{21}Na. This state has an angular momentum $J^\pi = 1/2^-$ and therefore it primary decay branches emits their gamma rays isotropically. In Fig. 30 a decay scheme of the resonance is shown with the branchings as given by [22].

3.4.1 Optimal energy and pressure

For the study of the E_R= 366 keV resonance, MC simulations where performed at both different pressures, P = 0.5, 1, 1.5, 2, 2.5 mbar, and different beam energies, E_{beam}= 384.6, 386, 388, 390, 392, 394, 396, 398, 400 keV. For each energy and pressure 10^7 events were generated at the resonance. The code generates the event distribution along the beam line based on the initial beam energy and target pressure. The information on energy loss and straggling are implemented based on TRIM [40] simulations at different energies and target densities. Based on Ziegler's data the initial beam energy E_{beam} necessary to populate the resonance ($E_{res,LAB} = 384.5$ keV) inside the target chamber at distance z from the collimator is well approximated by

$$E_{beam}(z) = b(p)z + a(p), \tag{49}$$

with

$$a(p) = 384.4520 - 0.715\,052\,6 \cdot p(\text{mbar}),$$
$$b(p) = 0.007\,151 + 0.263\,37 \cdot p(\text{mbar}).$$

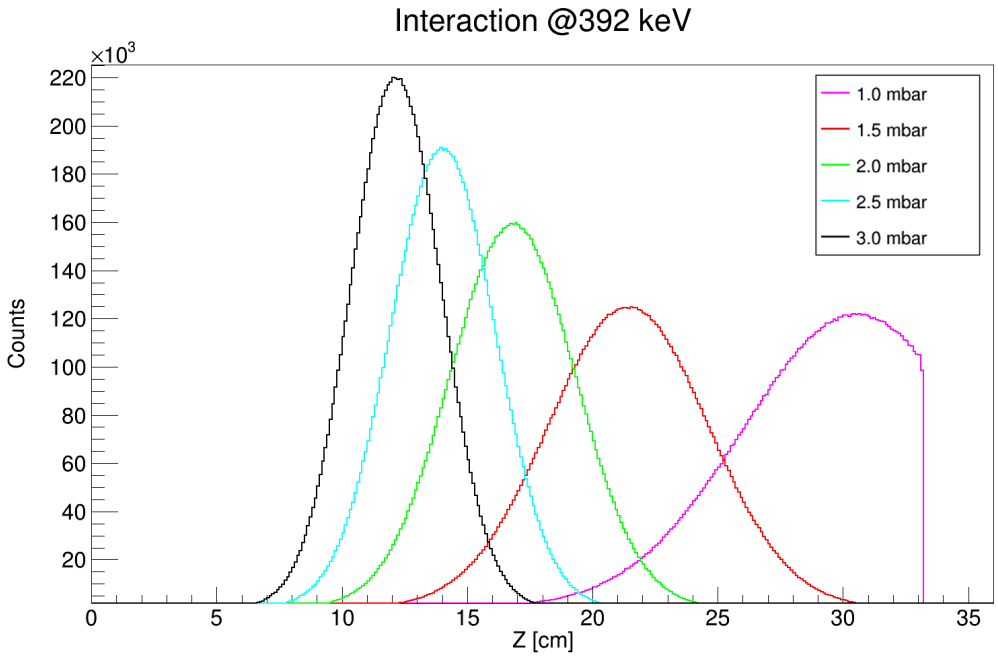

Figure 31: Distribution of the simulated events inside the chamber for E_{beam} =392 keV at different gas pressures, $z = 0$ is the end of the entrance collimator.

The energy straggling was also extrapolated via SRIM yielding the formula

$$\sigma_{stragg} = 0.366 \cdot \Delta E^{0.554}, \tag{50}$$

where $\Delta E = E_{beam} - E_{res,LAB}$.

The branchings implemented are the one given by Rolfs *et al.* [22] (Fig. 30). The γ-rays from the primary branches are emitted isotropically.

For the sake of simplicity, the target density inside the gas target is assumed to be constant and negligible before the collimator. Studies of the density profile have been conducted for this experimental setup [34] both with and without the beam (*beam heating effect*). These corrections might be applied during a later analysis.

Based on the examined ranges the condition $E_{beam} = 392$ keV and $P = 2$ mbar was chosen as a best-case to evaluate the expected efficiencies and count rates as in this condition the resonance is well contained inside the target chamber (see Fig. 31).

3.4.2 Count rate estimation

Fixed the experimental conditions for the Monte Carlo the simulation are run generating spectra for the 2 detectors given $N_{events} = 10^7$ (an example is shown in Fig. 32).

Considering the counts seen in the full energy peak for the different transitions, the total number of the simulated events and the yield formulas, the count rate can be estimated as:

$$A_\gamma/t = \frac{N(E_\gamma)}{N_{Events}} \frac{I}{e} \frac{\lambda^2}{2} \frac{m_p + m_t}{m_t} \frac{\omega\gamma}{\epsilon}, \tag{51}$$

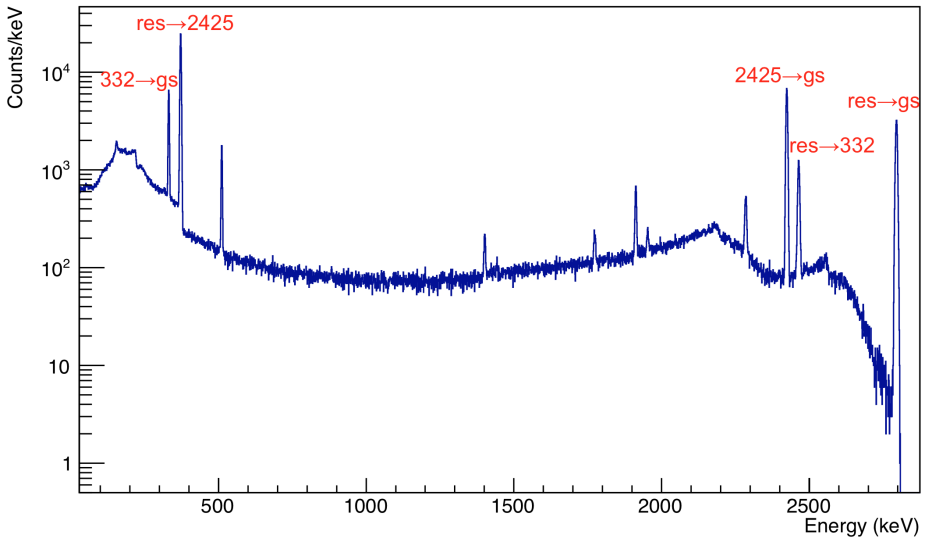

Figure 32: Example Monte Carlo spectrum for the direct capture with the relevant transitions.

where $N(E_\gamma)$ is the number of counts in the peak at energy E_γ, N_{Events} is the total number of generated events, I is the beam current in Ampere, e is the elementary charge in C, and ϵ is the energy loss in units of keV $\cdot$ cm^2/atoms. For E_{beam} =392 keV and P = 2 mbar the energy loss is $\epsilon = 10.791 \times 10^{-15}$ eV $\cdot$ cm^2/atoms. The 366 keV resonance strength is assumed to be the one given by Rolfs, $\omega\gamma = 0.11 \pm 0.02$ meV. The $\lambda^2/2$ is the De Broglie wavelength, calculated as in [2]:

$$\frac{\lambda^2}{2} = \left(\frac{m_p + m_t}{m_t}\right)^2 \frac{4.125 \times 10^{-18}}{m_p E_r{}^{lab}(eV)} = 1.175 \times 10^{-23} cm^2. \quad (52)$$

Assuming a beam current of $\sim$ 200 μA, it is possible to estimate the expected count rate for the different transitions. The results are reported in Tab. 3.

Transition	E_γ (keV)	GePD (counts/s)	time to 1% (h)	GeDD (counts/s)	time to 1% (h)
332 $\rightarrow$ gs	332	0.4	6.9	0.2	15
res $\rightarrow$ 2425	373	1.9	1.5	0.8	3.4
2425 $\rightarrow$ gs	2425	0.7	4.2	0.3	9.9
res $\rightarrow$ 332	2466	0.13	21.3	0.06	49.33
res $\rightarrow$ gs	2797	0.4	7.1	0.2	18.1

Table 3: Expected count rate and measure time expected to obtain 10 000 counts in the peak area (1% precision) for the different energies, at E_{beam}=392 keV, P = 2 mbar, assuming $\sim$ 200 μA current, neglecting the possible backgrounds.

This example shows that:

- All the transitions seems to be measurable within reasonable beam time at the LUNA facility.

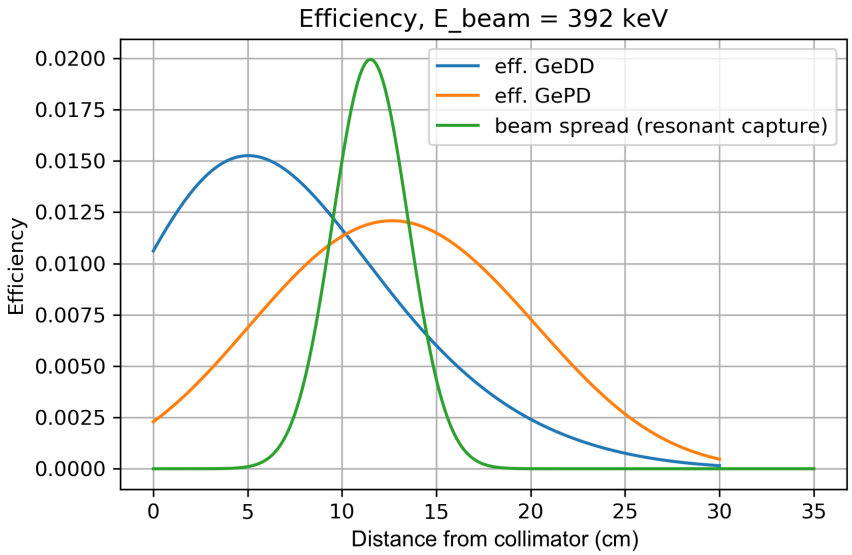

Figure 33: The efficiency profile of the two detectors along the beam line inside the gas target, compared to typical beam energy spread inside the target chamber. Here, only the resonant capture is populated at fixed energy, and the spread of the beam is determined by the beam energy straggling inside the gas target. As a consequence, the detectors see the photon from the reaction not from a fixed point but distributed over the beam line and this determines a loss in the detected yield.

- The counting rates expected are all higher than the expected background in their respective region of interest. See Fig.17 (full-shielding red spectrum) and Tab. 2.

All this consideration are meant to give mainly qualitative results, especially given that recent results report updated resonance strength and branchings for the resonance [23]. These claims will be eventually verified during the analysis of the future measurements.

3.5 ENERGY STRAGGLING MEASUREMENT

As we have seen in section 3.2, the beam energy straggling at the resonance can be estimated using the formula from Bohr (Eq. 34) or parameterizing this effect inside the gas target using TRIM simulations (see Eq. 50). Using the particular experimental configuration that will be mounted, it is also possible to extract this value of straggling from the measurements since the two detectors see the reaction from different positions and, as a consequence, the ratio between the counting rates of the detectors is sensible to the energy straggling. In Fig. 33 an example configuration is shown with typical beam spread at the resonance energy along with the detection efficiency profile of the two detector along the beam line in the gas target.

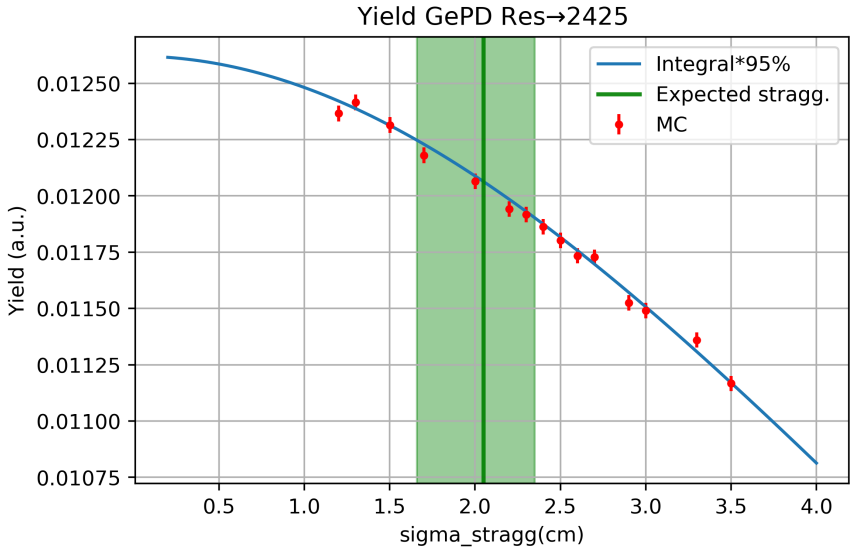

Figure 34: Yield for the res → 2425 transition as a function of the straggling for the lower detector (E_{beam}=392 keV, P = 2 mbar). The green bar identifies the range of straggling extracted from a measure of the ratio between the yields of the two detectors (Fig. 35), as explained on section 3.5.

Using the detection efficiency parametrization $\eta(E, z)$ obtained in section 3.1.2 it is possible to analytically determine the counts expected from N events simulated at the resonance as

$$N_{counts}(E_\gamma, \sigma_{stragg}) = \text{B.r.} \times \int_{z_{in}}^{z_{fin}} \eta(E_\gamma, z) \frac{N}{\sigma_{stragg}\sqrt{2\pi}} \exp\left(-\frac{(z-z_0)^2}{2\sigma^2_{stragg}}\right) dz \tag{53}$$

where z_0 is the point where the resonance is populated.

If the γ-ray is part of a cascade, eventual summing-in/summing-out effects should also be taken into consideration (i. e. an additional factor inside the integral, $(1-\eta_{T,2}(z)W(\theta))$ where $\eta_{T,2}(z)$ is the total detection efficiency for the second γ and $W(\theta)$ its angular distribution). Varying σ_{stragg} typically determine a loss of count with respect to the case where no straggling is taken into consideration.

From Eq. 53 it is possible to give an analytical parametrization of the counts expected changing σ_{stragg} and comparing it to the simulation, obtained by varying the straggling without changing the point in which the resonance is populated. Depending on each transition a correction ($\sim$ 5%) is applied to the numerical integration of Eq. 53 in order to correct for summing-in/summing-out effects. The correction is applied comparing the numerical integration to the corresponding Monte Carlo data.

In Fig. 34 the effect of varying the straggling is shown for a given transition at fixed beam energy. The shown yield is determined both analytically and with the simulations. As discussed in the previous paragraph, to match the data determined with Eq. 53 the correction is applied. As expected, if the resonance is populated in front of the detector, a loss of counts is determined with respect to the situation with no straggling.

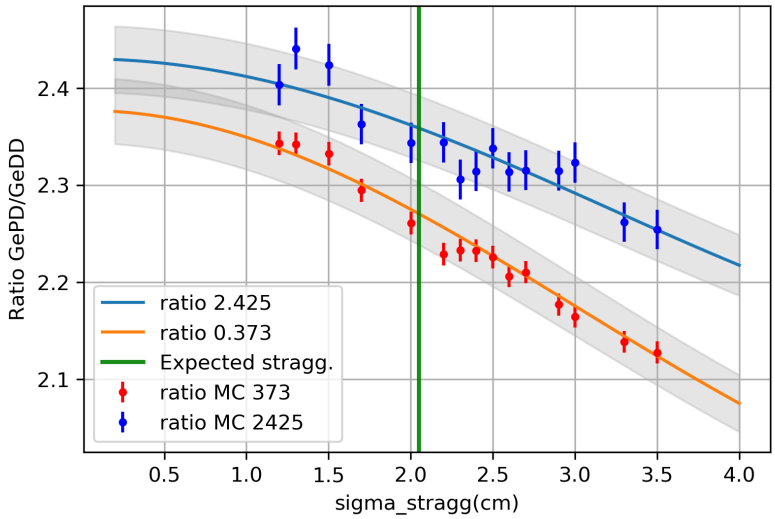

Figure 35: Ratio between the yield of the two detectors as a function of σ_{stragg}, for two different transitions (E_{beam}=392 keV, P = 2 mbar). The gray band represents the uncertainty obtainable in the estimate if the ratio of the two transitions are measured within 1% precision.

The ratio between the yields of the two detectors is then parametrized changing the energy straggling and compared in Fig. 35: for reference the gray band represents the uncertainty on the ratio obtained in case of 1% precision on the yields.

This roughly gives about half a centimeter precision in the determination of σ_{stragg}, which translates to $\sim$ 2% uncertainty on the measure of the resonance strength $\omega\gamma$. This is evaluated in the following way:

- The ratio of Fig. 35 is taken at the reference value for the straggling expected from Eq. 50 (2.05 cm at E_{beam}=392 keV) at the considered conditions.
- This value of the ratio determines two points in the gray bands that translate into a range for the straggling (i. e. [−19% - 14%] from the initial position for the 373 keV γ-ray).
- For this range of σ_{stragg} corresponds an interval of yields (see Fig. 34) that determines two values of $\omega\gamma$ (see Eq. 46).

The final resonance strength varies in the interval [−1.3% - 1.5%] for the 373 keV transition and in [−1.6% - 1.7%] for the 2425 keV transition.

The resonance is also populated at two other positions, corresponding to $E_{beam} = 390, 394$ keV, in order to further test the effect on the ratios. The results can be seen in Fig. 36,37. Between the two cases, populating the resonance midway the two detectors ($E_{beam} = 390$ keV) is by far the best option, as at 394 keV the resonance is populated far too distant from the GeDD and the statistics collected by the GeDD would be too small.

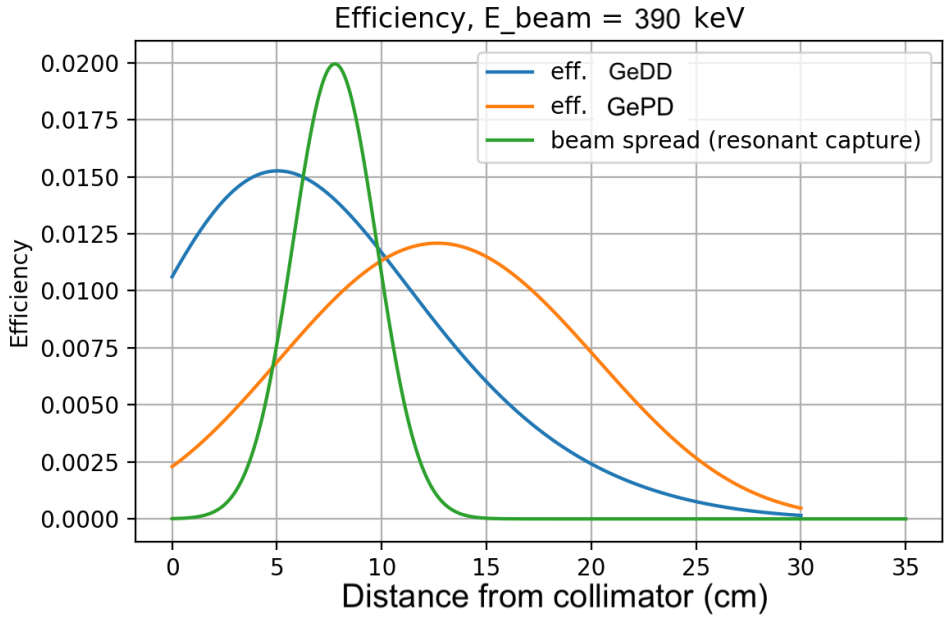

(a) Configuration

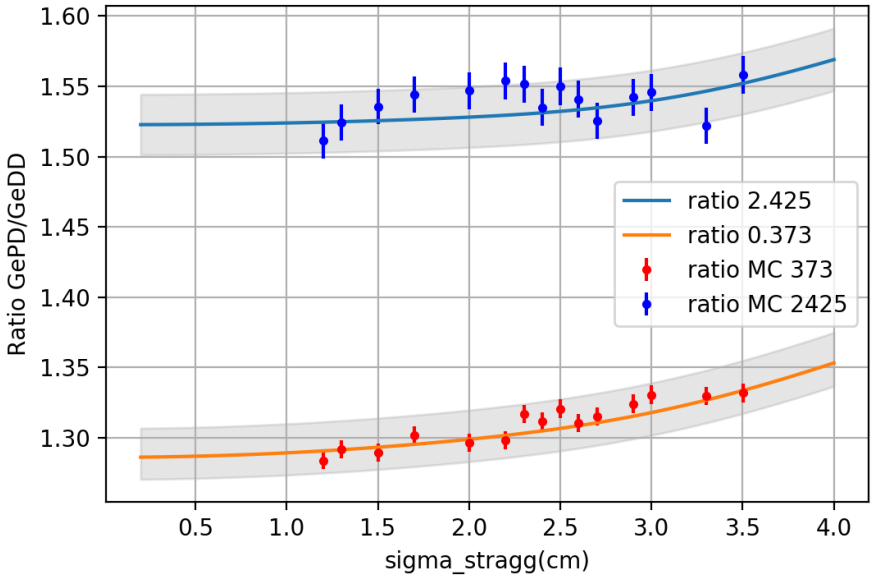

(b) Ratio

Figure 36: Ratios between the yields of the two detector for the configuration obtained setting $E_{beam} = 390$ keV.

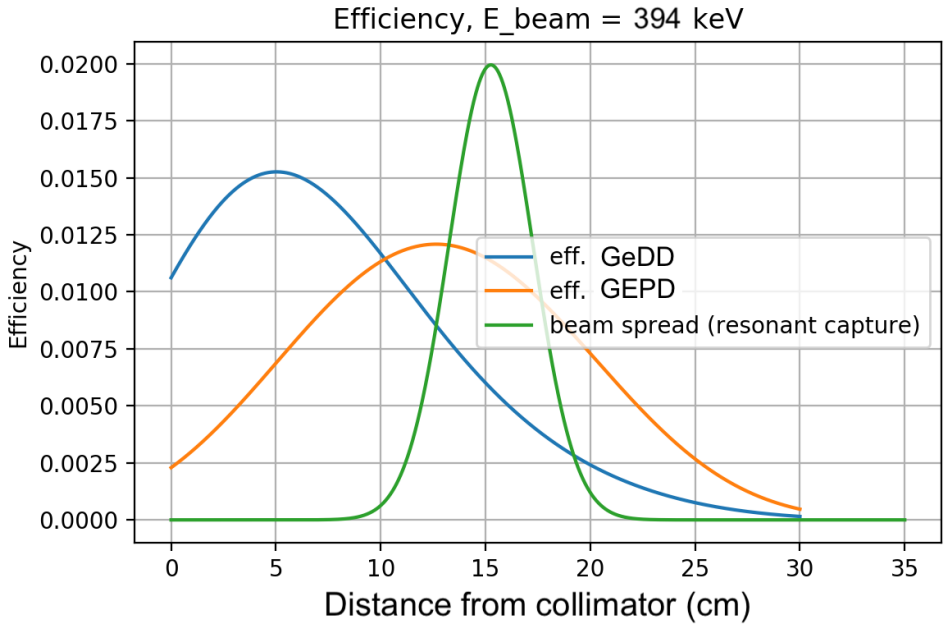

(a) Configuration

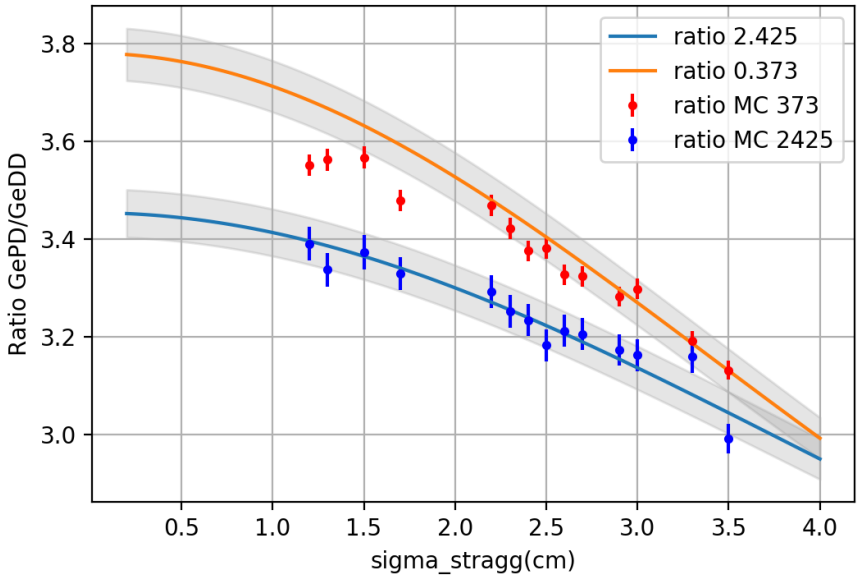

(b) Ratio

Figure 37: Ratios between the yields of the two detector for the configuration obtained setting $E_{beam} = 394$ keV. At low values of spread in straggling the ratio estimated numerically differs significantly from the MC. This is due to the uncertainty on the parametrization of the efficiency of the GEDD, at large distance from the maximum efficiency.

3.6 FINAL REMARKS

In the end, the simulations allowed to optimize the conditions for the future data taking. The main achievements of this study for the measurement of the reaction $^{22}Ne(p,\gamma)^{23}Na$ are briefly resumed:

- As a first step (Section 3.1.2), the geometry of the setup and the detectors were implemented in the GEANT-3 code and later fixed using the data available from a ^{60}Co source.
- A full parametrization of the efficiency inside the chamber was obtained for both detectors to be later used in the numerical computation of the effects in the gas target.
- Optimal conditions for data taking were determined. It was found that overall $E_{beam} = 392$ keV and $P = 2$ mbar are a good compromise to populate the reaction completely inside the chamber (Section 3.1.2).
- The expected count rate was determined using these conditions (Section 3.4.2). This result will be later used to better plan the data taking during the experiment.
- The effect of beam energy straggling inside the target chamber was studied using Monte Carlo simulation and numerical computation (Section 3.5). The effect on the yield of the two detectors was preliminary determined. The main result from this section was that the yields are not so sensible to small fluctuations in σ_{stragg}. This quantity can then be determined either analytically or by exploiting the ratio between the count rates from the two detectors.

4 CONCLUSION

The $^{20}Ne(p,\gamma)^{21}Na$ reaction was introduced in the context of nuclear astrophysics. In the first chapter the current literature for the reaction at low energies is reviewed, in particular in the recent years (2019), new direct measurements [23, 25] at low energies exposed significant discrepancies with the result of Rolfs *et al.* [22] (1975) especially for the strength and the branchings of the 366 keV resonance. These results, if confirmed, may lead to a decrease in the reaction rate in the range of temperatures of interest for oxygen-neon classical novae ([0.1 - 0.3] GK). The LUNA-400 accelerator is perfectly suited for the measurement of both the resonance and the direct capture component of the $^{20}Ne(p,\gamma)^{21}Na$ in conditions of unprecedentedly low background.

The experimental setup that will be used in the study of this reaction was presented in the second section along with the main challenges related to the measurement. The expected environmental background was reported and some possible sources of contamination from the beam induced background addressed.

Given the shutdown of the experimental activities imposed by the 2020 pandemic, the next part of the analysis focused more heavily on Monte Carlo. The code was validated using calibration spectra from the current setup and data from one of the previous campaigns. The final efficiency profile obtained differs by less than 2% with the data taken for the current setup. The second detector, not yet mounted, was positioned and calibrated in the MC using the old measurements. The final agreement is poorer (~8%) but can be improved once the detector will be mounted. A full parametrization of the efficiency $\eta(E,z)$ was then obtained simulating monoenergetical source.

The resonant capture was simulated at different beam energies and pressures inside the chamber. The expected counting rates were evaluated for the best conditions and compared to the expected background levels.

In the end, the method was proposed to independently measure the beam energy straggling inside the gas target. This possibility is explored using simulation and numerical calculations obtained using the efficiency parametrization obtained previously. This solution seems definitely promising since does not require any separate measure and the straggling uncertainty does not affect the yield nor the resonance strength that much (only a few percent). However, this method relies on a very precise determination of the efficiency for the real setup.

The LUNA collaboration is expected to resume the setup construction in Autumn 2020 followed by data taking later down the line.

BIBLIOGRAPHY

[1]M. E. Burbidge, G. Burbidge, W. A. Fowler, and F. Hoyle, "Synthesis of the elements in stars", Rev. Mod. Phys. **29**, 547–650 (1957).

[2]C. Iliadis, *Nuclear physics of stars* (Wiley, Hoboken, NJ, 2015).

[3]A. Anttila, J. Keinonen, and M. Bister, "The DSA lifetime of the 2425 keV state in21na", Journal of Physics G: Nuclear Physics **3**, 1241–1244 (1977).

[4]A. Boeltzig, C. G. Bruno, F. Cavanna, S. Cristallo, T. Davinson, R. Depalo, R. J. deBoer, A. Di Leva, F. Ferraro, G. Imbriani, and et al., "Shell and explosive hydrogen burning", The European Physical Journal A **52** (2016).

[5]M. Wiescher, J. Gorres, E. Uberseder, G. Imbriani, and M. Pignatari, "The cold and hot CNO cycles", Ann. Rev. Nucl. Part. Sci. **60**, 381–404 (2010).

[6]A. I. Karakas and J. C. Lattanzio, "The dawes review 2: nucleosynthesis and stellar yields of low- and intermediate-mass single stars", Publications of the Astronomical Society of Australia **31** (2014).

[7]B. Carroll and D. Ostlie, *An introduction to modern astrophysics* (Pearson Addison-Wesley, 2007).

[8]A. Renzini and M. Voli, "Advanced evolutionary stage of intermediate-mass stars. 1. Evolution of surface compositions.", Astron. Astrophys. **94**, 175–193 (1981).

[9]R. Gratton, C. Sneden, and E. Carretta, "Abundance variations within globular clusters", Ann. Rev. Astron. Astrophys. **42**, 385–440 (2004).

[10]I. I. Ivans, R. P. Kraft, C. Sneden, G. H. Smith, R. Rich, and M. Shetrone, "New analyses of star-to-star abundance variations among bright giants in the mildly metal-poor globular cluster m5", Astron. J. **122**, 1438 (2001).

[11]Carretta, E., Lucatello, S., Gratton, R. G., Bragaglia, A., and D´Orazi, V., "Multiple stellar populations in the globular cluster ngc 1851", A&A **533**, A69 (2011).

[12]D. Allen, "Classical novae m. f. bode and a. evans, (editors) john wiley and sons, 1989, 357 pp.", Publications of the Astronomical Society of Australia **8**, 229–229 (1989).

[13]J. Jose and M. Hernanz, "Nucleosynthesis in classical nova explosions", J. Phys. G **34**, R431–R458 (2007).

[14]J. B. Marion and W. A. Fowler, "Nuclear Reactions with the Neon Isotopes in Stars.", The Astrophysical Journal **125**, 221 (1957).

[15]R. M. Cavallo, A. V. Sweigart, and R. A. Bell, "Proton-capture nucleosynthesis in globular cluster red giant stars", The Astrophysical Journal **492**, 575–595 (1998).

[16]R. M. Cavallo, A. V. Sweigart, and R. A. Bell, "The production of sodium and aluminum in globular cluster red giant stars", The Astrophysical Journal **464**, L79–L82 (1996).

[17]A. Renzini, F. D'Antona, S. Cassisi, I. R. King, A. P. Milone, P. Ventura, J. Anderson, L. R. Bedin, A. Bellini, T. M. Brown, G. Piotto, R. P. van der Marel, B. Barbuy, E. Dalessandro, S. Hidalgo, A. F. Marino, S. Ortolani, M. Salaris, and A. Sarajedini, "The Hubble Space TelescopeUV Legacy Survey of Galactic Globular Clusters – V. Constraints on formation scenarios", Monthly Notices of the Royal Astronomical Society **454**, 4197–4207 (2015).

[18]F. Cavanna et al., "A new study of the ^{22}Ne(p,γ)^{23}Na reaction deep underground: Feasibility, setup, and first observation of the 186 keV resonance", Eur. Phys. J. A **50**, 179 (2014).

[19]K. J. Kelly, A. E. Champagne, L. N. Downen, J. R. Dermigny, S. Hunt, C. Iliadis, and A. L. Cooper, "New measurements of low-energy resonances in the ^{22}Ne(p,γ)^{23}Na reaction", Phys. Rev. C **95**, 015806 (2017).

[20]C. Iliadis, J. M. D'Auria, S. Starrfield, W. J. Thompson, and M. Wiescher, "Proton-induced thermonuclear reaction rates for a =20–40 nuclei", The Astrophysical Journal Supplement Series **134**, 151–171 (2001).

[21]S. Lyons et al., "Determination of Ne20(p,γ)Na21 cross sections from Ep=500-2000keV", Phys. Rev. C **97**, 065802 (2018).

[22]C. Rolfs, W. Rodne, M. Shapiro, and H. Winkler, "Hydrogen burning of 20 Ne and 22 Ne in stars", Nucl. Phys. A **241**, 460–486 (1975).

[23]A. L. Cooper, "A low-energy tudy of the 20ne(p,g)21na reaction with high current proton beam at lena", PhD thesis (University of North Carolina, Chapel Hill, 2019).

[24]A. Mukhamedzhanov et al., "Asymptotic normalization coefficients from the Ne20(He3, d)Na21 reaction and astrophysical factor for Ne20 (p,gamma) Na21", Phys. Rev. C **73**, 035806 (2006).

[25]J. Karpesky, "Measuring the neon-20 radiative proton capture rate at dragon", PhD thesis (Colorado School of Mines, 2020).

[26]C. Broggini, D. Bemmerer, A. Guglielmetti, and R. Menegazzo, "Luna: nuclear astrophysics deep underground", Annual Review of Nuclear and Particle Science **60**, 53–73 (2010).

[27]A. Best, A. Caciolli, Z. Fülöp, G. Gyürky, M. Laubenstein, E. Napolitani, V. Rigato, V. Roca, and T. Szücs, "Underground nuclear astrophysics: why and how", The European Physical Journal A **52** (2016).

[28]A. Caciolli et al., "Ultra-sensitive in-beam gamma-ray spectroscopy for nuclear astrophysics at LUNA", Eur. Phys. J. A **39**, 179–186 (2009).

[29]D. Bemmerer et al., "Feasibility of low energy radiative capture experiments at the LUNA underground accelerator facility", Eur. Phys. J. A **24**, 313–319 (2005).

[30]A. Formicola, G. Imbriani, M. Junker, D. Bemmerer, R. Bonetti, C. Broggini, C. Casella, P. Corvisiero, H. Costantini, G. Gervino, C. Gustavino, A. Lemut, P. Prati, V. Roca, C. Rolfs, M. Romano, D. Schürmann, F. Strieder, F. Terrasi, H.-P. Trautvetter, and S. Zavatarelli, "The luna ii 400kv accelerator", Nuclear Instruments and Methods in Physics Research Section A: Accelerators, Spectrometers, Detectors and Associated Equipment **507**, 609–616 (2003).

[31]F. Ferraro et al., "A high-efficiency gas target setup for underground experiments, and redetermination of the branching ratio of the 189.5 keV^{22}Ne(p, γ)^{23}Na resonance", Eur. Phys. J. A **54**, 44 (2018).

[32]F. Cavanna et al., "Three New Low-Energy Resonances in the $^{22}Ne(p,\gamma)^{23}Na$ Reaction", Phys. Rev. Lett. **115**, [Erratum: Phys.Rev.Lett. 120, 239901 (2018)], 252501 (2015).

[33]R. Depalo et al., "Direct measurement of low-energy ^{22}Ne(p,γ)^{23}Na resonances", Phys. Rev. C **94**, 055804 (2016).

[34]R. Depalo, "The neon-sodium cycle: study of the 22ne(p,gamma)23na reaction at astrophysical energies", PhD thesis (Universitá degli studi di Padova, 2015).

[35]R. Brun, F. Bruyant, M. Maire, A. McPherson, and P. Zanarini, "GEANT3", (1987).

[36]C. Casella et al., "First measurement of the d(p,γ) 3 He cross section down to the solar Gamow peak", Nucl. Phys. A **706**, 203–216 (2002).

[37]V. Mossa et al., "Setup commissioning for an improved measurement of the D(p,gamma)3He cross section at Big Bang Nucleosynthesis energies", Eur. Phys. J. A **56**, 144 (2020).

[38]G. F. Knoll, *Radiation detection and measurement; 4th ed.* (Wiley, New York, NY, 2010).

[39]N. B. D. Phil., "Lx. on the decrease of velocity of swiftly moving electrified particles in passing through matter", The London, Edinburgh, and Dublin Philosophical Magazine and Journal of Science **30**, 581–612 (1915).

[40]J. F. Ziegler, M. D. Ziegler, and J. P. Biersack, "SRIM - The stopping and range of ions in matter (2010)", Nuclear Instruments and Methods in Physics Research B **268**, 1818–1823 (2010).

[41]M. Mayer, "Simnra, a simulation program for the analysis of nra, rbs and erda", AIP Conference Proceedings **475** (1999).

[42]M. Mayer, "Simnra user's guide", Tech. rep. IPP 9/113, 103 (1997).

[43]H. E. Gove, "Resonance Reactions, Experimental", in Nuclear reactions, Vol. 1, edited by P. M. Endt and M. Demeur (Jan. 1959), p. 259.

[44]D. Bemmerer, F. Cavanna, R. Depalo, M. Aliotta, M. Anders, A. Boeltzig, C. Broggini, C. Bruno, A. Caciolli, and et al., "Effect of beam energy straggling on resonant yield in thin gas targets: the cases 22ne(p,g)23na and 14n(p,g)15o", EPL (Europhysics Letters) **122**, 52001 (2018).

[45]C. Iliadis, A. Champagne, J. Jose, S. Starrfield, and P. Tupper, "The effects of thermonuclear reaction-rate variations on nova nucleosynthesis: a sensitivity study", The Astrophysical Journal Supplement Series **142**, 105–137 (2002).